The role of thermal and non-thermal processes in the ISM of the Magellanic Clouds

H. Hassani [ORCID],[1,2]★ F. Tabatabaei,[2] A. Hughes [ORCID],[3,4] J. Chastenet,[5,6] A. F. McLeod [ORCID],[7,8] E. Schinnerer[9] and S. Nasiri[1]

[1]*Shahid Beheshti University, Faculty of Physics, Department of Astronomy and Astrophysics, 19839 Tehran, Iran*
[2]*School of Astronomy, Institute for Research in Fundamental Sciences (IPM), PO Box 19395-5531, Tehran, Iran*
[3]*CNRS, IRAP, 9 Av. du Colonel Roche, BP 44346, F-31028 Toulouse cedex 4, France*
[4]*Université de Toulouse, UPS-OMP, IRAP, F-31028 Toulouse cedex 4, France*
[5]*Center for Astrophysics and Space Sciences, Department of Physics, University of California, San Diego, 9500 Gilman Drive, La Jolla, CA 92093, USA*
[6]*Sterrenkundig Observatorium, Ghent University, Kri-jgslaan 281-S9, B-9000 Gent, Belgium*
[7]*Department of Astronomy, University of California Berkeley, Berkeley, CA 94720, USA*
[8]*Centre for Extragalactic Astronomy, Department of Physics, Durham University, South Road, Durham DH1 3LE, UK*
[9]*Max-Planck-Institut für Astronomie, Königstuhl 17, D-69117 Heidelberg, Germany*

ABSTRACT

Radio continuum emission is a dust-unbiased tracer of both thermal and non-thermal processes in the interstellar medium. We present new maps of the free–free and synchrotron emission in the Magellanic Clouds (MCs) at 0.166, 1.4, and 4.8 GHz with no prior assumption about the radio non-thermal spectrum. The maps were constructed using a de-reddened $H\alpha$ map as a template for the thermal radio emission, which we subtract from maps of the total radio continuum emission. To de-redden the $H\alpha$ emission, it is important to know the fraction of dust surface density that attenuates the $H\alpha$ emission along the line of sight, f_d. This fraction is obtained by comparing the dust opacity obtained through the infrared emission spectrum and the Balmer decrement method. In star-forming regions, the median f_d is about 0.1, which is lower than that in diffuse regions by a factor of three. We obtain a global thermal radio fraction, f_{th}, of 30 per cent (35 per cent) in the LMC (SMC) at 1.4 GHz. Furthermore, we present maps of the equipartition magnetic field strength with average values of $\simeq 10.1\,\mu G$ in the LMC and $\simeq 5.5\,\mu G$ in the SMC. The magnetic field is proportional to the star-formation rate to the power of 0.24 and 0.20 for the LMC and SMC, respectively. This study shows that non-thermal processes control the interstellar medium in the MCs.

Key words: radio continuum: galaxies – ISM: general – ISM: magnetic fields – radiation mechanisms: thermal – radiation mechanisms: non-thermal – galaxies: irregular.

1 INTRODUCTION

The radio continuum (RC) emission observed from astrophysical sources is dominated by non-thermal (synchrotron) and thermal (free–free) emission at frequencies $\lambda < 10\,GHz$ (Condon 1992). The thermal emission originates from the warm ionized nebular medium (e.g. H II regions) with a typical electron temperature of $T_e \simeq 10^4\,K$ and often has a flat power-law radio spectral energy distribution $S_\nu = \nu^{-0.1}$ (e.g. Filipovic et al. 1998; Draine 2011). The non-thermal emission is due to cosmic ray electrons (CREs) accelerated by the magnetic field in the interstellar medium (e.g. supernova remnants) and is described by a power-law spectrum with a variable non-thermal spectral index α_n ($S_\nu = \nu^{\alpha_n}$). Interaction and energy loss of CREs in different environments (e.g. spiral arms of galaxies or their nuclei) change the non-thermal spectral index α_n (Longair 2011). Hence, assuming a constant α_n in resolved studies can underestimate or overestimate the synchrotron emission depending on the medium. For instance, assuming $\alpha_n = -1$ results in an underestimation of

both the non-thermal emission (by >30 per cent; Tabatabaei et al. 2007) and the magnetic field strength in massive star-forming regions. Avoiding such assumptions, several attempts have been made to map the pure synchrotron emission in nearby galaxies, including M33, M31, NGC 6946, and NGC 1097 (Tabatabaei et al. 2013a, b; 2018). Separating the thermal and non-thermal emission is the first step towards understanding the origin of the well known correlation between the RC and infrared (IR) continuum emission in galaxies (van der Kruit 1971; de Jong et al. 1985; Helou, Soifer & Rowan-Robinson 1985). It is also vital in studying the energy balance and structure formation in the interstellar medium (ISM) of galaxies.

The MCs, our nearest-neighbour galaxies, provide ideal laboratories for detailed ISM studies in low-mass and low-metallicity systems. The Large Magellanic Cloud (LMC) is at a distance of 49.9 kpc (Pietrzynski et al. 2019) with an almost face-on view that hosts one of the brightest and most complex extragalactic H II regions, 30 Doradus (hereafter 30 Dor). Being located about 62.4 kpc from our Sun (Graczyk et al. 2020), the Small Magellanic Cloud (SMC) is farther away and more inclined ($i = 64°$; see e.g. Subramanian & Subramaniam 2015) than the LMC. These inclinations mean that

★ E-mail: hamid@Ipm.ir, hhassani@ualberta.ca

Table 1. General parameters adopted for the MCs.

LMC	
Centre (J2000)	RA = $05^h23^m34^s$ Dec. = $-69°45'22''$
Inclination[1]	$34.0°$
Distance[2]	49.9 kpc (1 arcsec = 0.24 pc)
SMC	
Centre (J2000)	RA = $00^h52^m44^s$ Dec. = $-72°49'42''$
Inclination[3]	$64.4°$
Distance[4]	62.4 kpc (1 arcsec = 0.30 pc)

Note. References: [1]van der Marel & Kallivayalil (2014). [2]Pietrzynski et al. (2019). [3]Subramanian & Subramaniam (2015). [4]Graczyk et al. (2020).

the distances reported can change up to 10 per cent from one end to the other of each galaxy. Some general properties of the MCs are summarized in Table 1.

They have been extensively studied in the RC in both total power (Loiseau et al. 1987; Klein et al. 1989; Haynes et al. 1991; For et al. 2018; Joseph et al. 2019; Pennock et al. 2021) and polarization (Klein et al. 1993; Gaensler et al. 2005; Mao et al. 2008, 2012). The *Herschel Space Observatory* and the *Spitzer Space Telescope* have made major breakthroughs in studies of the dust and gas in the MCs (Meixner et al. 2006, 2013; Gordon et al. 2011; Lakićević et al. 2015). Moreover, nebular emission line maps from both the LMC and the SMC are available through optical observations such as the Magellanic Clouds Emission Line Survey (MCELS; Smith & MCELS Team 1999; Smith et al. 2005; Points, Smith & Chu 2005; Pellegrini et al. 2012; Winkler et al. 2015).

Several attempts have been made to study the RC emission components in the MCs, mostly using a fixed α_n across the galaxies (hereafter called the classical separation method). Klein et al. (1989) obtained $\alpha_n = -0.84$ and found a thermal fraction of $f_{th} = 55$ per cent at 1.4 GHz for the LMC. Hughes et al. (2006) studied the radio–IR correlation separately for the thermal and non-thermal RC assuming $\alpha_n = -0.7$ and found a tight correlation in regions with a high thermal fraction.

The structure and strength of the magnetic fields in the MCs have been studied by several authors (Klein et al. 1993; Gaensler et al. 2005; Mao et al. 2008, 2012). In the LMC, an average magnetic field along the line of sight of $\simeq 4.3 \mu G$ was obtained through Faraday rotation studies (Gaensler et al. 2005). Using the classical thermal/non-thermal separation technique, Klein et al. (1989) reported an equipartition field strength of $\simeq 6 \mu G$ in the same galaxy. In the SMC, Mao et al. (2008) found a galactic-scale mean field strength of $\simeq 0.2 \mu G$ along the line of sight and a random field strength of $\simeq 3 \mu G$ in the sky plane. However, no full map of the magnetic field strength in the MCs is available for studying its role in the ISM energy balance and structure formation. The ordered magnetic field is shown to be smaller in dwarf galaxies than in spiral galaxies (Chyży et al. 2011), indicating that a large-scale dynamo process may not maintain the production of the magnetic field in dwarf galaxies. As the small-scale dynamo originates from the injection of turbulent energy from supernova explosions, massive stars may play a primary role in dwarf galaxies such as the MCs. Such a small-scale dynamo can be investigated through its power-law relation with star formation (Schleicher & Beck 2013). Chyży et al. (2011) finds such correlations for dwarf galaxies in global studies. Mapping the magnetic field strength is necessary to address these relations in the MCs, taking advantage of our close distance to the MCs and hence inspecting these questions at a physical resolution of less than 80 pc for the first time.

The paper aims to study the thermal and non-thermal properties of the ISM, map the total magnetic field strength, and investigate its correlation with the star-formation rate (SFR) in the MCs. Using recent Murchison Widefield Array (Lonsdale et al. 2009; Bowman et al. 2013; Tingay et al. 2013) low-frequency observations as well as archival ATCA and Parkes data (Haynes et al. 1986; Filipovic et al. 1995, 1996, 1997; Kim et al. 1998, 2003), we present full maps of the thermal and non-thermal emission for both the LMC and the SMC.

Unlike the classical separation method, we do not assume a fixed α_n to obtain the thermal and non-thermal RC maps. We use the thermal radio template (TRT) technique developed for NGC 6946 (Tabatabaei et al. 2013a). This method uses a recombination line such as Hα emission to trace the thermal free–free emission. In this work, to de-redden the Hα emission, no assumption for the fraction of dust attenuating the emission (f_d) is applied, unlike our previous studies. We determine f_d for the MCs by comparing the dust mass obtained using the Balmer-line-decrement ratio method (e.g. Cardelli, Clayton & Mathis 1989; Calzetti et al. 2000) with that extracted from dust-emission spectral energy distribution (SED) studies. Hence, this paper presents distributions of the thermal and non-thermal RC emission across the MCs more precisely than before.

The data are described in Section 2. In Section 3, we determine f_d for a sample of H II regions as well as for more diffuse regions and present a general f_d calibration relation using its correlation with neutral gas. In Section 4, we present thermal and non-thermal maps at different frequencies at an angular resolution of 221 arcsec ($\sim$53 pc) for the LMC and 235 arcsec ($\sim$71 pc) for the SMC. Non-thermal spectral index maps are presented in Section 5. After mapping the magnetic field strength, we investigate its correlation with the SFR at different spatial resolutions, compare the thermal and non-thermal energy densities of the ISM, and discuss the propagation of CREs in Section 6.

2 DATA

The data used in this study are summarized in Table 2. The MCs were observed with the Murchison Widefield Array (MWA) telescope (Lonsdale et al. 2009; Tingay et al. 2013) as part of the Galactic Extragalactic All-Sky MWA (GLEAM) survey in the frequency range of 0.074–0.231 GHz (Wayth et al. 2015). The data reduction is explained in detail by Hurley-Walker et al. (2016). Due to slight changes in ionospheric conditions, a point spread function (PSF) map is created for each mosaic with a variation of 15–20 per cent across each field. We used the radio continuum at 0.166 GHz with a robust 0 weighting from For et al. (2018). Calibration uncertainty in the flux density is 8.5 per cent for the LMC and 13 per cent for the SMC (Hurley-Walker et al. 2016).

At higher frequencies, the LMC and the SMC have been observed with the Australia Telescope Compact Array (ATCA) and the Parkes telescope at 1.4 GHz and 4.8 GHz by several authors (Dickel et al. 2005, 2010; Hughes et al. 2007; Crawford et al. 2011; Wong et al. 2011a). For the LMC, we used the merged ATCA+Parkes data at 1.4 GHz and 4.8 GHz as presented by Hughes et al. (2007) and Dickel et al. (2005), respectively. We assume a calibration uncertainty of 6.5 per cent at 1.4 GHz and 8.5 per cent at 4.8 GHz for the LMC data. For the SMC, we used these observations only at 1.4 GHz assuming a 5 per cent calibration uncertainty (Wong et al. 2011a). The quality and signal-to-noise ratio of the available RC data for the SMC are much poorer at 4.8 GHz (Dickel et al. 2010; Crawford et al. 2011) than at 1.4 GHz. The rms noise value of the RC map is about 2.6 times higher at 4.8 GHz than at 1.4 GHz. We note that, in the SMC, the signal-to-noise ratio is lower that that in the LMC by a factor of two at 4.8 GHz. These data are also severely affected by artefacts around

Table 2. Images of the Magellanic Clouds used in this study.

Frequency	Angular resolution (arcsec)	rms	Ref.	Telescope
LMC				
0.166 GHz	221×221	0.02 (Jy beam^{-1})	For et al. (2018)	MWA
1.4 GHz	40×40	0.30 (mJy beam^{-1})	Hughes et al. (2007)	ATCA+Parkes
4.8 GHz	33×33	0.30 (mJy beam^{-1})	Dickel et al. (2005)	ATCA+Parkes
6563 Å (Hα)	4.6×4.6	0.12 (10^{-15} erg s^{-1} cm^2)	Smith & MCELS Team (1999)	UM/CTIO
70 µm	18×18	0.41 (MJy sr^{-1})	Meixner et al. (2006)	*Spitzer*/MIPS
CO (1–0)	45×45	0.40 (K km s^{-1})	Wong et al. (2011b, 2017)	Mopra
H I – 21 cm	60×60	15 (mJy beam^{-1})	Kim et al. (2003)	ATCA+Parkes
4800–9300 Å (IFU)	$\simeq 0.4 \times 0.4$	–	Bacon et al. (2010)	MUSE/VLT
SMC				
0.166 GHz	235×235	0.02 (Jy beam^{-1})	For et al. (2018)	MWA
1.4 GHz	98×98	1.50 (mJy beam^{-1})	Wong et al. (2011a)	ATCA+Parkes
6563 Å (Hα)	4.6×4.6	0.01 (10^{-17} erg s^{-1} cm^2)	Smith & MCELS Team (1999)	UM/CTIO
70 µm	18×18	0.47 (MJy sr^{-1})	Gordon et al. (2011)	*Spitzer*/MIPS
4800–9300 Å (IFU)	$\simeq 0.4 \times 0.4$	–	Bacon et al. (2010)	MUSE/VLT

bright sources. These prevent the study of low-surface-brightness regions of the SMC, which is the main area of interest in this study. Hence, we opt not to use these data at 4.8 GHz for the SMC.

The Hα map of the MCs was taken through the MCELS survey (Smith & MCELS Team 1999; Winkler et al. 2015). This survey covers the central $8 \times 8°$ of the LMC and $4.5 \times 3.5°$ of the SMC. It used a Curtis Schmidt telescope with a pixel size of 2.3 arcsec (Smith & MCELS Team 1999). The Hα maps were continuum subtracted for the entire mosaic, rather than field-by-field using two continuum band filters as detailed in Paredes et al. (2015). We masked several bright background point sources with Hα flux about 100 times higher than in H II regions as they seem to suffer from saturation in the reduction process. We use a calibration uncertainty of 10 per cent for the Hα maps provided by the MCELS Team (private communication).

Absolute photometry of Hα and Hβ for 74 (27) H II regions in the LMC (SMC) has been reported by Caplan & Deharveng (1985) and Caplan et al. (1996) (hereafter Caplan catalogue). Photometry measurements were taken in circular apertures of 4.89, 2.00, and 1.06 arcmin diameters. These aperture sizes are adopted to ensure integration over the full H II regions and for comparison with the Parkes radio continuum data at 4.8 GHz. The LMC Hα/Hβ flux ratio and its emission lines suffer from 4 per cent uncertainty in random errors, imprecise atmospheric attenuation, and other systematic errors. However, the uncertainty in the Hα/Hβ flux ratio is estimated to be about 7 per cent in the SMC (Caplan & Deharveng 1985; Caplan et al. 1996).

The MCs were observed with *Herschel* and *Spitzer* in different bands from 3.6–500 µm by the HERITAGE and SAGE projects (Meixner et al. 2006, 2010, 2013, 2015; Gordon et al. 2011). Chastenet et al. (2019) modelled the FIR dust emission using the Draine & Li (2007) dust model. We use their total dust-mass surface-density maps with an angular resolution of 36 arcsec.

The 21 cm H I line emission was observed with ATCA and Parkes (Kim et al. 2003) and the CO (1–0) line emission is provided by the Magellanic Mopra Assessment (MAGMA) survey (Wong et al. 2011b, 2017) for the LMC.

We use optical IFU MUSE/VLT observations toward several fields in the MCs (see Fig. 1), including H II regions and supernova remnants (SNRs) to investigate the extinction properties of the diffuse gas in SNRs versus star-forming regions. These data were taken in wide-field mode (WFM) with a field of view of ≈1 arcmin and are summarized in Table 3. The two H II regions of the LMC

are reduced and mosaicked by McLeod et al. (2018). Our sample of MUSE SNR fields was taken from the Phase 3 ESO Science Archive and reduced using ESO's automatic pipeline (Weilbacher, Streicher & Palsa 2016). We note that this automatic pipeline may oversubtract emission lines and produce artificial absorption lines in the spectrum. Comparing the MUSE SNR Hα flux with the MCELS survey data in a 1 arcmin rectangular aperture shows an agreement within <18 per cent of the total flux. We take an extra 20 per cent uncertainty in flux of the emission line ratio ($F_{H\alpha}/F_{H\beta}$) for the sky oversubtraction effect in the LMC SNRs. We did not find any noticeable absorption lines in the integrated spectra or each pixel of the SNR 1E0102−7219.

All maps were convolved to the lowest common resolution of our data sets, 221×221 arcsec for the LMC and 235×235 arcsec for the SMC, using Gaussian kernels. The smoothed maps were then regridded to a common astrometric grid. We considered not only the rms noise (σ_{rms}) of the observed maps but also the calibration uncertainty (σ_{cal}) of the instruments to estimate uncertainties in fluxes (following $\sigma = \sqrt{\sigma_{rms}^2 + \sigma_{cal}^2}$). These errors were then propagated to obtain uncertainties in other parameters reported throughout the paper.

3 EXTINCTION IN THE MAGELLANIC CLOUDS

The *Herschel* and *Spitzer* space telescopes have made a major breakthrough in mapping the dust content of galaxies. These observations can be used to map extinction and de-redden the optical Hα emission provided that the relative distribution of emitting sources and dust particles is known along the line of sight (Tabatabaei et al. 2013a). A uniform mix of dust and ionized gas emitting Hα requires half of the total dust mass (or optical depth) to be considered in de-reddening. A smaller fraction must be used in the more realistic case of non-uniformity, such as a smaller z-distribution of dust than ionized gas (Dickinson, Davies & Davis 2003) or due to clumpiness. As follows, the total dust opacity is first obtained in the MCs. Then we derive the fraction of it that is linked to reddening of the Hα emission (f_d) by comparing the total dust optical depth with true extinction obtained using the Hα-to-Hβ ratio method. This is done for H II regions and a few MUSE fields including more diffuse ISM. Moreover, a calibration relation for f_d is obtained by investigating its correlation with neutral gas surface density across the LMC.
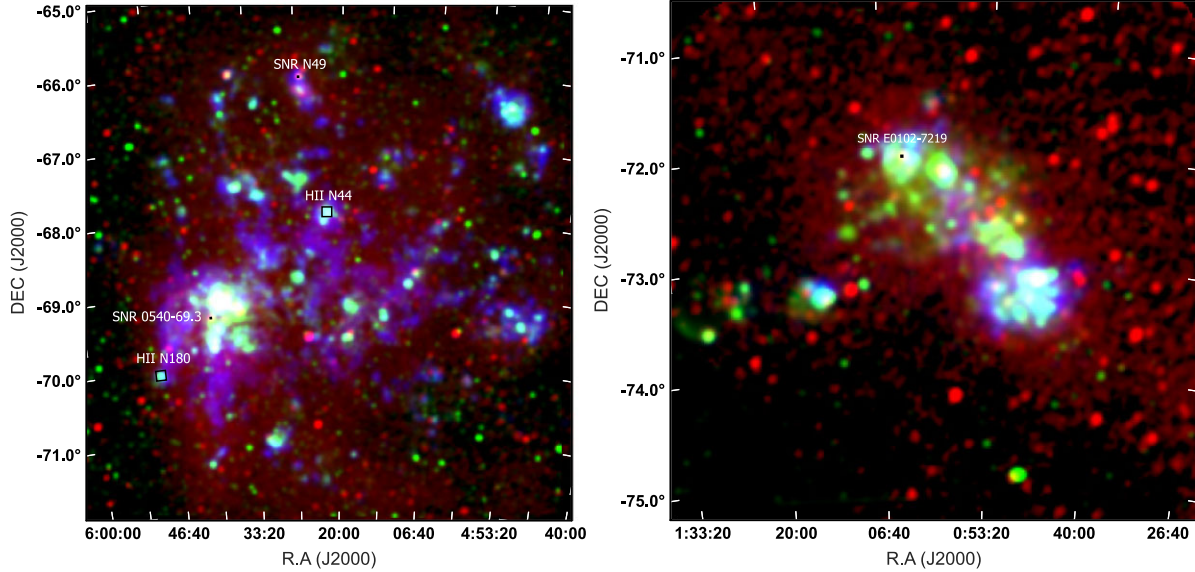
Figure 1. Three-colour composite images of the Large Magellanic Cloud (left) and the Small Magellanic Cloud (right) showing the radio continuum emission at 0.166 GHz from the GLEAM survey on a log scale (red), the Hα emission from the MCELS survey on a linear scale (green), and the dust-mass surface density from Chastenet et al. (2019) on a log scale (blue). Black squares show the MUSE/VLT observed fields.

Table 3. MUSE/VLT observed fields in the MCs.

Name	RA (J2000)	Dec. (J2000)	Area	Programme ID	Ref.
LMC/N44	80.534	−67.936	8 × 8 arcmin	096.C-0137(A)	McLeod et al. (2018)
LMC/N49	81.505	−66.083	60 × 60 arcsec	0100.D-0037(A)	J. T. Van Loon[1]
LMC/SNR 0540−69.3	85.046	−69.332	60 × 60 arcsec	0102.D-0769(A)	J. Lyman[1]
LMC/N180	87.206	−70.055	8 × 8 arcmin	096.C-0137(A)	McLeod et al. (2018)
SMC/1E0102−7219	16.012	−72.031	60 × 60 arcsec	297.D-5058(A)	Vogt et al. (2017)[1]

Note. [1]Data retrieved from the ESO Phase 3 Archive.

3.1 Dust opacity

Using the *Herschel* and *Spitzer* data, Chastenet et al. (2019) mapped different dust properties including dust-mass surface density in the MCs based on the DL07 model (Draine & Li 2007). A composition of carbonaceous and amorphous silicates was assumed for dust grains, which are heated by a variable radiation field U with a delta-function distribution. Taking a fixed U_{max} = 10^7 U$_\odot$, the minimum interstellar radiation-field intensity spans a range of 0.1 U$_\odot$ ≤ U_{min} < 50 U$_\odot$. Considering the Galactic R_V = 3.1 (Cardelli et al. 1989), dust SEDs were fitted based on this model from 3.6−500 μm. This results in 36 arcsec resolution maps of dust-mass surface density Σ_d with a pixel size of 14 arcsec for the MCs. This leads to a dust optical depth following $\tau_{dust} = \kappa_\Sigma \Sigma_d$, where κ_Σ is the dust opacity. At the Hα wavelength, $\kappa_\Sigma = 1.4701 \times 10^4$ cm^2 g^{-1} for the LMC and $\kappa_\Sigma = 1.2026 \times 10^4$ cm^2 g^{-1} for the SMC (Weingartner & Draine 2001; Gordon et al. 2003) taking into account both absorption and scattering by dust grains.

Examining the τ_{dust} map obtained reveals a mean τ_{dust} = 1.08 ± 0.04 within a 5° radius centred on (5^{h}23^m, −69°45′)$_{J2000}$ for the LMC. It is τ_{dust} = 0.48 ± 0.02 within a 3° radius centred on (0^{h}52^m, −72°49′)$_{J2000}$ in the SMC. In other words, the SMC's ISM is more transparent to the Hα emission than the LMC, since it has a relatively lower dust-mass surface density Σ_d < 0.1 and metallicity (see Jameson et al. 2016 and references therein).

3.2 Effective extinction

The dust optical depth obtained in Section 3.1 can be used to de-redden the observed Hα emission if the emitting sources (here ionized gas) are all behind a slab of dust with that optical depth (τ_{dust}). However, in reality, ionized gas and dust are mixed and hence only a fraction of τ_{dust} must be considered. This fraction depends on the relative distributions of ionized gas and dust along the line of sight, which are often unknown. Following Dickinson et al. (2003) and Tabatabaei et al. (2013a) we define an effective dust optical depth that should be considered to obtain the true extinction. It is given by the multiplication of τ_{dust} by the factor f_d that is the fraction of dust attenuating the Hα emission along the line of sight:

$$\tau_{eff} \equiv f_d \times \tau_{dust} \tag{1}$$

with τ_{eff} as the effective dust optical depth obtained at the Hα wavelength. We note that τ_{eff} in terms of visual extinction, A_V, is given by:

$$\tau_{eff} = \frac{A_V \kappa_{H\alpha}}{1.086 R_V} \tag{2}$$

with a total to selective ratio R_V = 3.41 for the LMC and 2.74 for the SMC (Gordon et al. 2003). Dickinson et al. (2003) found that f_d = 0.33 can best reproduce the Galactic plane's observed data, interpreting it as demonstrating that only a third of the dust along the line of sight is responsible for reddening. As the distribution of

the ISM in dwarf systems can be different from normal-mass spiral galaxies, we expect that f_d also differs. Hence, we try to estimate f_d using observations of the Balmer decrements.

We use the Hα and Hβ emission data to measure the extinction using the following relations (e.g. Cardelli et al. 1989; Calzetti et al. 2000):

$$E(B - V)_{\text{Balmer}} = \frac{2.5}{\kappa(\text{H}\beta) - \kappa(\text{H}\alpha)} \log_{10}\left(\frac{F_{\text{H}\alpha}/F_{\text{H}\beta}}{2.86}\right) \quad (3)$$

$$A_{\text{V}} = R_{\text{V}}\, E(B - V)_{\text{Balmer}} \quad (4)$$

with $E(B - V)$ the reddening and $F_{\text{H}\alpha}$, $F_{\text{H}\beta}$ the intrinsic Hα and Hβ fluxes. We adopted the theoretical $F_{\text{H}\alpha}/F_{\text{H}\beta} = 2.86$ (Brocklehurst 1971; Osterbrock 1989).

Using the Calzetti et al. (2000) attenuation law, we obtain $\kappa(\text{H}\alpha)$ and $\kappa(\text{H}\beta)$ as 2.72 and 4.40 for the LMC and 2.19 and 3.76 for the SMC. Considering that A_{V} from equation (2) must be equal to that given by equation (4), f_d is obtained separately for the H II regions and diffuse ISM as follows.

3.2.1 Calibrating f_d in H II regions

The $F_{\text{H}\alpha}$ and $F_{\text{H}\beta}$ fluxes were extracted from the Caplan catalogue for a sample of 74 H II regions in the LMC and 25 H II regions in the SMC. We first derive their visual extinction A_{V} using equations (3) and (4). Extracting τ_{dust} for the apertures in the Caplan catalogue, we then calibrate and obtain f_d using equation (2). The A_{V} changes between 0.09 and 1.03 for the LMC with a median value of $A_{\text{V}} = 0.35$, which is larger by 34 per cent than in the SMC. Uncertainties in the observed fluxes affect A_{V} by less than 0.09 mag in the LMC and 0.14 mag in the SMC. The dust filling factor f_d obtained using equation (2) varies between 0.02 and 0.46 for the LMC and between 0.01 and 0.72 for the SMC with a median value of $f_d \simeq 0.1$ in both the LMC and the SMC H II regions (green bars in Fig. 2). Tables 4 and 5 list the resulting visual extinction A_{V}, dust-mass surface density Σ_d, and f_d.

Using the Caplan catalogue we can only derive an average f_d in H II regions, but taking advantage of the MUSE observations we can map f_d in the two H II regions N44 and N180 (McLeod et al. 2018). We take a 32 Å wide (Hα + N II) line based on MUSE observations covering an 8×8 arcmin area centred at $(5^\text{h}48^\text{m}49\overset{\text{s}}{.}46, -70^\circ03'19''53)_{\text{J2000}}$ and $(5^\text{h}22^\text{m}08\overset{\text{s}}{.}13, -67^\circ56'08''26)_{\text{J2000}}$ for N180 and N44, respectively. Details of the spectral extraction are found in McLeod et al. (2018). We performed aperture photometry on the Hα and Hβ emission lines in N44 and N180 for each MUSE pixel resulting in a map of f_d (Fig. 3), indicating a good agreement with our integrated measurement within a 4.89 arcmin diameter circular aperture of the Caplan catalogue, $f_d = 0.06$ and $f_d = 0.11$ in N44BC and N180AB. We note that the integrated Hα flux increases by about 20 per cent adopting the (Hα + N II) bandwidth in comparison with the slab of the narrow 6 Å Hα line. Inspecting the f_d maps, it is inferred that clumps of dust corresponding to dense regions of molecular gas have lower f_d than more diffuse regions (Fig. 4, top left).

3.2.2 Calibrating f_d in the diffuse ISM

Determining f_d and τ_{eff} should not be limited to only dense ionized gas in the H II regions because there is a considerable amount of Hα emission from lower-density regions in the MCs. In this section, we use the MUSE observations of a few SNRs (see Table 3) as they represent more diffuse regions than the H II regions. Using a Gaussian fit, we first derive the centre of each specific emission line (listed in Table 6), and then we obtain zero moments of the Hα line with a
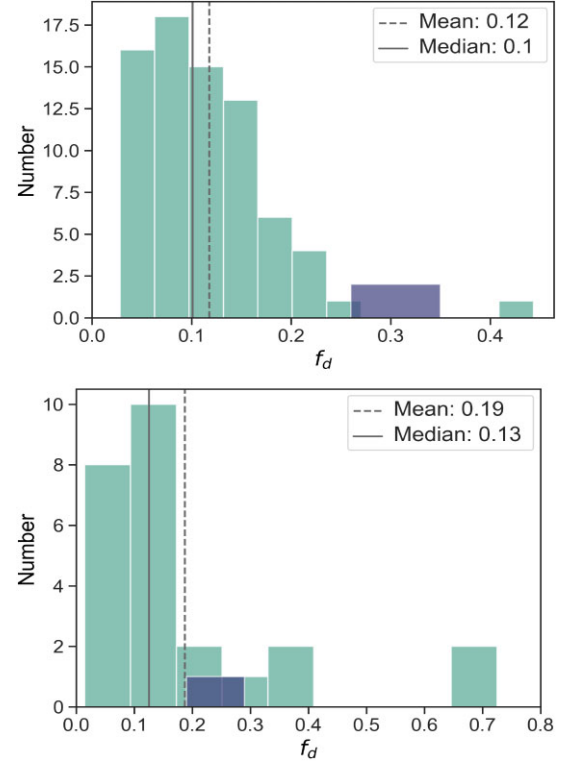

Figure 2. A histogram of f_d in H II regions (green) and diffuse regions (purple) for the LMC (top) and the SMC (bottom).

32 Å width and the Hβ line using a 6 Å width slab on each central line. The resulting f_d is higher in the SNRs by a factor of around three compared to the H II regions, indicating that dust is better mixed with the ionized gas in the SNRs than in the H II regions (purple bars in Fig. 2). In other words, as dust is clumpier in the H II regions than in the SNRs, the dust filling factor is smaller in the H II regions. Table 6 shows the resulting visual extinction A_{V}, dust-mass surface density Σ_d, and f_d for the MUSE/VLT fields.

Maps of f_d could only be derived for a few H II regions and SNRs using MUSE observations. To map the variation of f_d for the entire galaxy, its correlation with the total neutral gas is first investigated for the given fields and sources (Fig. 4, top left). Then a calibration relation is built to map f_d over the entire galaxy. We measured the total gas surface density as $\Sigma_{\text{gas}} = \Sigma_{\text{H I}} + \Sigma_{\text{H}_{\text{mol}}}$ where $\Sigma_{\text{H}_{\text{mol}}} = 2\,N(\text{H}_2) = 2\,X_{\text{CO}} \times I_{\text{CO}}$ and adopting a conversion factor $X_{\text{CO}} = 2 \times 10^{20}\,\text{cm}^{-2}\,(\text{K km s}^{-1})^{-1}$ (Strong & Mattox 1996). A similar conversation factor $X_{\text{CO}} \approx 2.76 \times 10^{20}\,\text{cm}^{-2}\,(\text{K km s}^{-1})^{-1}$ was reported for the LMC (Leroy et al. 2011). Excluding pixels weaker then 3σ rms ($\sigma = 3.3 \times 10^{19}\,\text{H cm}^{-2}$) in total gas surface density, we found a relation between f_d and Σ_{gas} in the LMC:

$$\text{Log } f_d\,(\text{LMC}) = (-0.62 \pm 0.04)\,\text{Log }\Sigma_{\text{gas}} - (0.67 \pm 0.03). \quad (5)$$

We then construct a synthesized map for f_d using equation (5) in the LMC (Fig. 4, top right). In the H II regions, the median value of f_d is about 0.1, which agrees with the more direct estimate outlined in Section 3.2.1 with a mean $\Sigma_{\text{gas}} = 3 \times 10^{21}\,\text{H cm}^{-2}$. This factor is higher in regions of lower-density gas ($\Sigma_{\text{gas}} < 8 \times 10^{20}\,\text{H cm}^{-2}$) as expected. We found a mean value $f_d = 0.29 \pm 0.04$ in the LMC within 5° of the central point $(5^\text{h}23^\text{m}34^\text{s}, -69^\circ45'22'')_{\text{J2000}}$, which is in good agreement with the Galactic value (Dickinson et al. 2003).

Table 4. Dust surface density (Σ_d), visual extinction (A_V), the fraction of dust attenuating Hα emission (f_d), and thermal fractions at 0.166 GHz ($f_{th}^{0.166\,GHz}$) and 1.4 GHz ($f_{th}^{1.4\,GHz}$) obtained for H II regions in the LMC. The Balmer-line-decrement ratio ($F_{H\alpha}/F_{H\beta}$) and the sizes of the sources are taken from Caplan & Deharveng (1985).

Source	R.A (J2000) (deg)	Dec. (J2000) (deg)	Radius (arcmin)	$F_{H\alpha}/F_{H\beta}$	Σ_d (10^{-5} g cm^{-2})	A_V	f_d	$f_{th}^{0.166\,GHz}$ (%)	$f_{th}^{1.4\,GHz}$ (%)
N77E	72.444	−69.199	4.89	3.52	16.73 ± 0.69	0.46	0.14 ± 0.03	20.4 ± 3.5	80.2 ± 10.1
N4AB	72.977	−66.907	4.89	3.24	19.62 ± 0.61	0.28	0.07 ± 0.02	46.1 ± 8.7	69.6 ± 9
N79AB	72.931	−69.398	4.89	3.78	17.63 ± 0.52	0.61	0.17 ± 0.03	28.2 ± 4.2	64.3 ± 8.1
N79DE	73.061	−69.345	4.89	3.50	22.91 ± 0.49	0.45	0.10 ± 0.02	36.3 ± 5.5	94.8 ± 12.1
N81	73.195	−69.224	4.89	3.65	14.72 ± 0.66	0.54	0.18 ± 0.03	−	127.7 ± 16.8
N83A	73.494	−69.200	4.89	3.77	24.77 ± 0.79	0.61	0.12 ± 0.02	55.8 ± 8.4	79.3 ± 10.3
N83 north	73.596	−69.154	2.00	3.68	19.24 ± 0.55	0.56	0.14 ± 0.02	98.2 ± 16	83.8 ± 10.6
N11F	74.164	−66.522	4.89	3.17	18.99 ± 0.53	0.23	0.06 ± 0.02	126.9 ± 20.4	117.1 ± 15
N11B	74.201	−66.404	4.89	3.36	30.22 ± 0.89	0.35	0.06 ± 0.01	137.2 ± 20.3	101 ± 13.2
N91	74.291	−68.415	4.89	3.42	14.70 ± 0.53	0.39	0.13 ± 0.03	17.1 ± 2.7	111.1 ± 14.1
N11CD	74.428	−66.461	4.89	3.21	28.33 ± 0.77	0.25	0.04 ± 0.02	130.5 ± 19.3	103.8 ± 13.4
N11E	74.535	−66.362	4.89	3.36	22.68 ± 0.55	0.35	0.08 ± 0.02	87.4 ± 14.9	82.8 ± 10.5
N23A	76.222	−68.056	4.89	3.28	8.56 ± 0.42	0.30	0.18 ± 0.05	−	89.6 ± 11.1
N103B	77.178	−68.764	4.89	3.24	9.92 ± 0.49	0.28	0.14 ± 0.04	11.4 ± 1.6	44.5 ± 5.5
N103A	77.344	−68.768	2.00	3.17	11.06 ± 0.68	0.23	0.10 ± 0.04	−	48.4 ± 6.1
N105A	77.477	−68.891	4.89	3.28	28.19 ± 0.78	0.30	0.05 ± 0.02	77.6 ± 11.2	74.9 ± 9.6
N113 south	78.340	−69.365	4.89	3.16	24.44 ± 0.58	0.22	0.04 ± 0.02	56.8 ± 8.2	90.4 ± 11.3
N113 north	78.397	−69.301	4.89	3.27	10.89 ± 0.50	0.29	0.14 ± 0.04	65.2 ± 9.5	92.2 ± 11.4
N119	79.663	−69.236	4.89	3.04	13.93 ± 0.34	0.13	0.05 ± 0.03	100.5 ± 14.5	118.9 ± 15
N120 (SNR)	79.643	−69.648	2.00	2.98	11.68 ± 0.37	0.09	0.04 ± 0.04	−	54.2 ± 6.7
N120AB	79.751	−69.637	2.00	3.06	26.49 ± 0.31	0.15	0.03 ± 0.02	−	71.3 ± 8.8
N120ABC	79.817	−69.653	4.89	3.14	17.48 ± 0.48	0.21	0.06 ± 0.03	40.6 ± 5.7	75.6 ± 9.3
N44BC	80.503	−67.970	4.89	3.33	33.73 ± 0.73	0.34	0.05 ± 0.01	62.6 ± 8.9	70.5 ± 8.9
N44I	80.609	−67.896	4.89	3.14	21.40 ± 0.56	0.21	0.05 ± 0.02	42.9 ± 6.1	59 ± 7.5
N44D	80.686	−68.076	4.89	3.44	32.21 ± 0.79	0.41	0.06 ± 0.01	−	65.9 ± 8.3
N138A	81.238	−68.480	4.89	3.44	19.78 ± 0.60	0.41	0.10 ± 0.02	−	69.7 ± 8.8
N48B	81.396	−66.304	4.89	3.64	16.24 ± 0.67	0.53	0.16 ± 0.03	8.5 ± 1.2	20.3 ± 2.5
N51D	81.508	−67.499	4.89	2.99	5.22 ± 0.39	0.10	0.09 ± 0.09	93.3 ± 13.8	104.8 ± 12.8
N51E	81.600	−67.622	4.89	3.31	6.65 ± 0.50	0.32	0.24 ± 0.07	26.5 ± 4.2	88.8 ± 10.9
N143	81.598	−69.315	4.89	3.14	4.86 ± 0.35	0.21	0.21 ± 0.09	13.6 ± 2.1	83.8 ± 10.5
N144AB	81.637	−68.825	4.89	3.47	17.67 ± 0.56	0.43	0.12 ± 0.03	114 ± 16.9	128.3 ± 16.6
N144	81.635	−68.863	4.89	3.46	9.43 ± 0.50	0.42	0.22 ± 0.05	94.2 ± 14.1	123 ± 15.6
N144	81.745	−68.825	4.89	3.45	9.97 ± 0.51	0.41	0.21 ± 0.05	102.9 ± 15.3	130 ± 16.6
N51C	81.901	−67.455	4.89	3.11	12.37 ± 0.54	0.18	0.07 ± 0.04	85.4 ± 12.8	110.8 ± 13.8
N51A	82.002	−67.424	4.89	3.21	16.21 ± 0.52	0.25	0.08 ± 0.03	49.7 ± 7.4	104.6 ± 13.2
N206	82.400	−71.001	4.89	3.51	5.10 ± 0.30	0.45	0.44 ± 0.09	−	87.9 ± 10.9
N206	82.587	−71.101	4.89	3.46	17.00 ± 0.60	0.42	0.12 ± 0.03	68.9 ± 10.3	81.7 ± 10.3
N206A	82.805	−71.069	4.89	3.46	21.29 ± 0.59	0.42	0.10 ± 0.02	81.5 ± 11.7	83.5 ± 10.5
N148	82.937	−68.532	4.89	3.34	25.23 ± 0.63	0.34	0.07 ± 0.02	−	78.5 ± 10.2
N55 north	83.024	−66.411	4.89	3.23	16.02 ± 0.53	0.27	0.08 ± 0.03	119.4 ± 22.7	128.4 ± 16.8
N55A	83.118	−66.467	4.89	3.21	14.59 ± 0.41	0.25	0.09 ± 0.03	147.6 ± 25.7	133.5 ± 17.3
N57A	83.099	−67.694	4.89	3.41	31.55 ± 0.58	0.39	0.06 ± 0.01	65.2 ± 9.8	124.4 ± 16.4
N57C	83.290	−67.713	4.89	3.42	18.64 ± 0.48	0.39	0.11 ± 0.02	−	88.6 ± 11.4
Filaments	83.353	−67.453	4.89	3.00	11.08 ± 0.49	0.10	0.05 ± 0.04	37.4 ± 5.6	69.7 ± 8.7
N154 south	83.725	−69.798	4.89	3.20	9.70 ± 0.48	0.25	0.13 ± 0.05	37 ± 5.2	66.7 ± 8.2
N63A	83.892	−66.031	4.89	3.19	8.61 ± 0.44	0.24	0.14 ± 0.05	−	18.5 ± 2.3
N59A	83.840	−67.585	4.89	3.84	24.33 ± 0.50	0.65	0.13 ± 0.02	97.9 ± 14.2	75.5 ± 9.7
N59B	83.986	−67.577	4.89	3.48	21.81 ± 0.59	0.43	0.10 ± 0.02	66.8 ± 9.7	75.6 ± 9.7
N157	83.952	−69.210	4.89	3.83	32.62 ± 0.78	0.64	0.10 ± 0.01	29.2 ± 4.2	52.5 ± 6.8
N157	84.086	−69.205	4.89	3.70	18.51 ± 0.45	0.57	0.15 ± 0.02	29.3 ± 4.1	54.2 ± 6.9
N154A	83.973	−69.646	4.89	3.35	23.51 ± 0.68	0.35	0.07 ± 0.02	62.6 ± 8.9	86.6 ± 11
N157	84.177	−69.216	4.89	3.69	23.89 ± 0.73	0.56	0.12 ± 0.02	31.9 ± 4.5	58.3 ± 7.4
N64AB	84.274	−66.361	4.89	3.23	18.44 ± 0.58	0.27	0.07 ± 0.02	64.6 ± 11.5	112.6 ± 14.6
N157B	84.449	−69.165	4.89	4.22	41.44 ± 0.72	0.86	0.10 ± 0.01	43.1 ± 6.8	47.6 ± 6.6
N157A – 30 Dor	84.660	−69.088	4.89	4.57	44.22 ± 3.32	1.03	0.12 ± 0.01	110.4 ± 21.9	65.6 ± 9.8
N158C	84.769	−69.506	4.89	3.62	35.33 ± 0.39	0.52	0.07 ± 0.01	73.2 ± 10.7	87 ± 11.4
N159A	84.908	−69.771	1.06	4.01	71.59 ± 1.08	0.74	0.05 ± 0.01	47.2 ± 6.6	37.7 ± 4.8
N16OAD	84.926	−69.646	4.89	3.73	51.23 ± 0.95	0.58	0.06 ± 0.01	6.6 ± 1	65.4 ± 8.7
N158	84.955	−69.441	4.89	3.34	17.32 ± 0.40	0.34	0.10 ± 0.03	43.4 ± 6.1	70.2 ± 8.8
N159	84.988	−69.752	4.89	4.09	53.88 ± 1.05	0.79	0.07 ± 0.01	28.9 ± 4.1	42.5 ± 5.5
N159BD	84.989	−69.733	2.00	4.24	56.16 ± 1.25	0.87	0.08 ± 0.01	−	46.5 ± 6.1
N159C	85.025	−69.756	1.06	3.59	68.06 ± 0.14	0.50	0.04 ± 0.01	50.3 ± 7.2	41.4 ± 5.4
N158A	85.040	−69.376	4.89	3.30	7.19 ± 0.45	0.32	0.22 ± 0.06	17.8 ± 2.4	36.2 ± 4.4
N16OBCE	85.046	−69.667	4.89	3.47	33.74 ± 0.54	0.43	0.06 ± 0.01	−	89.7 ± 11.7
N158	85.151	−69.412	4.89	3.25	7.68 ± 0.41	0.28	0.18 ± 0.06	21.3 ± 2.9	41.6 ± 5
N175	85.180	−70.041	4.89	3.52	11.55 ± 0.45	0.46	0.20 ± 0.04	12.4 ± 1.8	28.8 ± 3.6
Filaments	85.331	−69.084	4.89	3.37	10.20 ± 0.57	0.36	0.18 ± 0.04	20.5 ± 2.8	48.8 ± 6
N214C	85.410	−71.337	4.89	3.29	10.72 ± 0.43	0.31	0.14 ± 0.04	10.2 ± 1.5	75.3 ± 9.1
NGC 2100	85.526	−69.211	4.89	3.19	9.96 ± 0.64	0.24	0.12 ± 0.04	17.5 ± 2.4	47.5 ± 5.8
N164	85.648	−69.068	4.89	3.83	20.90 ± 0.38	0.64	0.15 ± 0.02	37.1 ± 5.2	62.7 ± 7.8
N165	85.723	−68.947	4.89	3.43	12.88 ± 0.55	0.40	0.16 ± 0.04	−	37.1 ± 4.6
N163	85.770	−69.759	4.89	3.89	23.30 ± 0.45	0.68	0.15 ± 0.02	10.2 ± 1.4	49 ± 6.1
N74A	86.427	−67.149	4.89	3.04	9.44 ± 0.53	0.13	0.07 ± 0.05	−	126.8 ± 23
N180AB	87.215	−70.071	4.89	3.30	23.07 ± 0.56	0.32	0.07 ± 0.02	63.9 ± 9.3	106.1 ± 13.4

Table 5. Dust surface density (Σ_d), visual extinction (A_V), the fraction of dust attenuating Hα emission (f_d), and thermal fractions at 0.166 GHz ($f_{th}^{0.166\,GHz}$) and 1.4 GHz ($f_{th}^{1.4\,GHz}$) obtained for H II regions in the SMC. The Balmer-line-decrement ratio ($F_{H\alpha}/F_{H\beta}$) and the sizes of the sources are taken from Caplan & Deharveng (1985).

| Source	RA (J2000) (deg)	Dec. (J2000) (deg)	Radius (arcmin)	$F_{H\alpha}/F_{H\beta}$	Σ_d (10^{-5} g cm^{-2})	A_V	f_d	$f_{th}^{0.166\,GHz}$ (%)	$f_{th}^{1.4\,GHz}$ (%)
N13AB	11.347	−73.380	4.89	3.51	15.60 ± 0.30	0.39	0.15 ± 0.05	27.5 ± 5.8	59.3 ± 6.3
N12Ba	11.387	−73.080	4.89	3.42	5.63 ± 0.48	0.34	0.37 ± 0.15	39.1 ± 8.2	87.6 ± 10.1
N12Ab	11.629	−73.101	4.89	3.34	11.86 ± 0.39	0.29	0.15 ± 0.07	–	71.5 ± 7.4
N19	11.932	−73.134	4.89	3.46	15.37 ± 0.14	0.36	0.14 ± 0.05	–	56.1 ± 5.3
N22	12.004	−73.270	2.00	3.46	24.31 ± 0.17	0.36	0.09 ± 0.03	53 ± 9.6	75.4 ± 7.1
N25–N26	12.029	−73.237	1.06	3.78	31.18 ± 0.44	0.53	0.10 ± 0.03	51.5 ± 9.6	79.8 ± 7.6
N24	12.040	−73.329	2.00	3.15	15.57 ± 0.27	0.18	0.07 ± 0.05	–	51 ± 5.1
N27	12.088	−73.099	2.00	3.43	37.23 ± 0.36	0.34	0.06 ± 0.02	–	84.7 ± 7.8
N28	12.148	−73.254	2.00	3.29	10.18 ± 0.20	0.26	0.16 ± 0.08	40.3 ± 7.3	72.6 ± 7.2
N30	12.240	−73.129	4.89	3.45	17.92 ± 0.07	0.35	0.12 ± 0.04	31.4 ± 5.6	79.7 ± 7.7
N36cg	12.616	−72.884	4.89	3.16	6.26 ± 0.45	0.19	0.18 ± 0.13	44.5 ± 8.3	92.7 ± 10
N37dg	12.687	−72.780	4.89	3.40	2.88 ± 0.28	0.33	0.69 ± 0.29	23.6 ± 4.4	81.5 ± 9.2
N66i	14.619	−72.195	4.89	3.08	9.97 ± 0.22	0.14	0.09 ± 0.08	–	91.6 ± 9.5
N66ii	14.771	−72.178	4.89	3.08	11.84 ± 0.28	0.14	0.07 ± 0.07	20.5 ± 3.5	78.2 ± 8
N66iii	14.771	−72.178	1.06	2.93	19.13 ± 0.07	0.05	0.01 ± 0.04	–	76.6 ± 7.7
N66iv	14.858	−72.165	4.89	3.13	8.09 ± 0.30	0.17	0.13 ± 0.10	32.7 ± 5.6	68.2 ± 7.1
N76	15.902	−72.057	4.89	3.04	12.01 ± 0.27	0.12	0.06 ± 0.07	29.5 ± 5.2	65.3 ± 6.6
N78ii	16.285	−71.993	4.89	3.35	6.10 ± 0.47	0.30	0.30 ± 0.13	–	66.1 ± 7.2
N80	17.106	−71.999	4.89	2.96	3.42 ± 0.45	0.07	0.12 ± 0.24	30.3 ± 7	79.8 ± 9.7
N81	17.284	−73.202	4.89	2.97	1.07 ± 0.13	0.07	0.41 ± 0.76	–	129.8 ± 24.6
N83A	18.451	−73.301	2.00	3.04	13.29 ± 0.26	0.12	0.05 ± 0.06	–	115.4 ± 11.9
N83	18.456	−73.288	4.89	3.28	13.07 ± 0.38	0.26	0.12 ± 0.06	–	111.8 ± 11.7
N84C	18.567	−73.266	1.06	3.91	20.59 ± 0.43	0.59	0.18 ± 0.04	–	105.4 ± 10.4
N84AB	18.681	−73.322	4.89	3.19	11.26 ± 0.36	0.21	0.11 ± 0.07	–	117.7 ± 12.8
N85fg	18.931	−73.334	4.89	3.17	1.65 ± 0.30	0.25	0.72 ± 0.51	–	84 ± 11.2
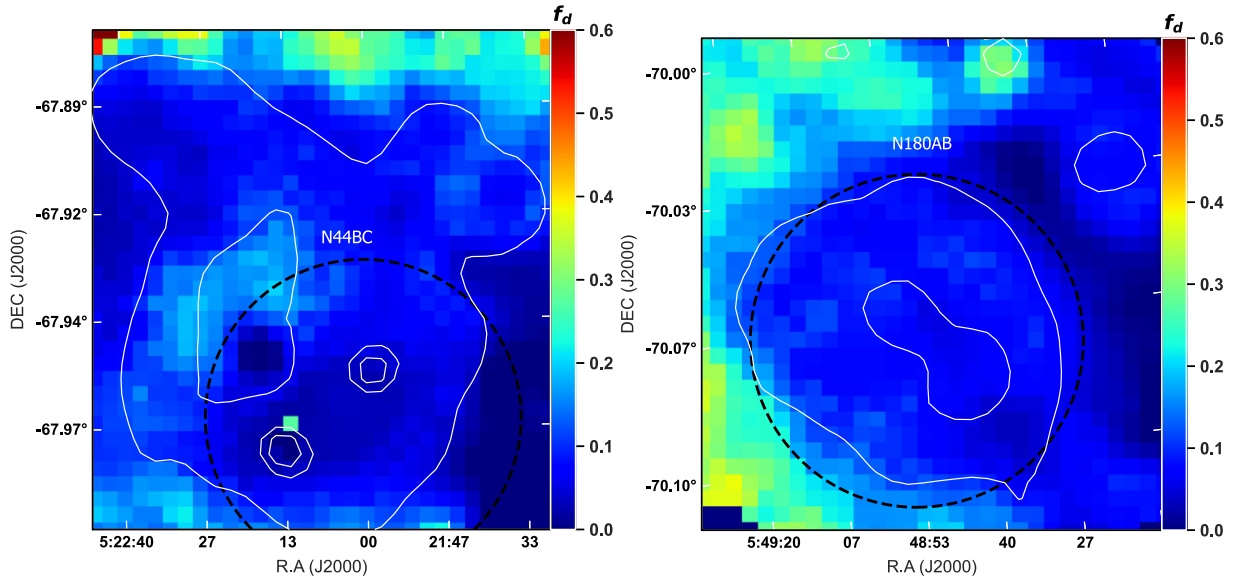
Figure 3. Map of the fraction of dust attenuating Hα emission f_d in the H II regions N44 (left) and N180 (right), overlaid with the Hα emission contours (white). Contours levels are 1, 6, and 8 × 10^{-16} erg s^{-1} cm^2 (left) and 1, 3, and 6 × 10^{-16} erg s^{-1} cm^2 (right). Black dashed circles are the apertures reported by Caplan & Deharveng (1985).

However, we should note that we found a variation of 0.2–0.3 in different ISM gas regimes.

We note that no correlation is found between f_d and neutral gas in the SMC, and hence no calibration relation can be extracted, perhaps due to the lack of a deep and full-coverage CO map. Thus, we take the median value of $f_d = 0.1$ to map the extinction in the SMC. In diffuse regions where it is expected to have deviations from $f_d = 0.1$, changing f_d from 0.1 to 0.3 affects (increases) the intrinsic Hα and hence the thermal fraction by less than 22 per cent as in these regions $\tau_{\mathrm{eff}} < 1$.
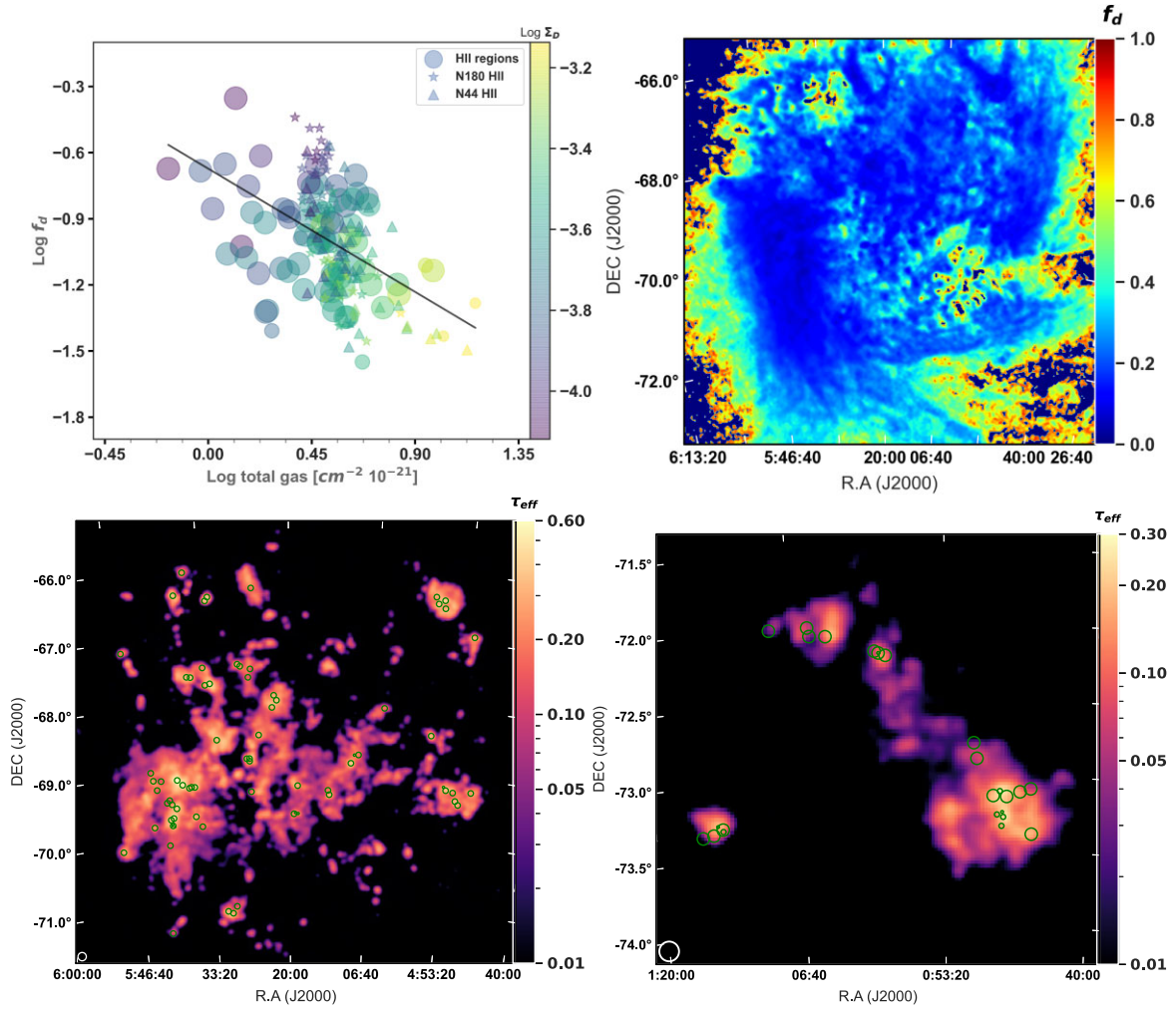
Figure 4. Top: the fraction of dust attenuating Hα emission f_d versus the total gas density Σ_{gas} (left) in separate fields and the map of f_d (right) in the LMC. Solid line shows the ordinary least-squares (OLS) bisector fit in log–log space used as an independent calibration of f_d. Bottom: effective dust optical depth (τ_{eff}) at the Hα wavelength for the LMC (left) and the SMC (right) shown on a log scale. Green circles indicate the position of H II regions inside the MCs. The beam sizes of 221 arcsec (for the LMC) and 235 arcsec (for the SMC) are shown in the lower left-hand corners of the maps.

3.2.3 *Extinction maps and de-reddening the Hα emission*

Fig. 4 (bottom row) shows the final maps of the effective extinction τ_{eff}. In the LMC, we find on average $\tau_{eff} = 0.08 \pm 0.01$ compared to $\tau_{eff} = 0.05 \pm 0.02$ in the SMC. Maximum extinction occurs in the centre of 30 Dor with $\tau_{eff} = 0.75 \pm 0.11$. We use the extinction map to de-redden the Hα map and obtain the intrinsic Hα intensity I_0 using $I = I_0 e^{-\tau_{eff}}$.

Adopting the extinction map τ_{eff} to de-redden Hα yields $\simeq$ 20 per cent obscuration for the LMC. This is higher than that in the SMC ($\simeq$ 4 per cent) and similar to the correction factor for the dust obscuration reported for M33 ($\simeq$ 13 per cent; Tabatabaei et al. 2007). Integration of the dust-corrected Hα map out to a radius of 5° yields an intrinsic Hα luminosity $L_{H\alpha} = (3.67 \pm 0.47) \times 10^{40}$ erg s^{-1} for the LMC. The SMC has a luminosity of $L_{H\alpha} = (6.87 \pm 1.06) \times 10^{39}$ erg s^{-1} out to a radius of 3.5°.

4 SEPARATION OF THERMAL AND NON-THERMAL RADIO EMISSION

Separating the thermal and non-thermal radio emission is critical to study cosmic ray energy-loss mechanisms and the total magnetic fields. A pure non-thermal synchrotron spectral index map can be obtained using the TRT method, in which the thermal (free–free) emission is obtained using the de-reddened Hα emission as its template (Tabatabaei et al. 2013a).

4.1 From Hα emission to radio free–free emission

The Hα intensity is related to the emission measure (EM) depending on the transparency of the ISM to Lyman continuum photons. In case of the ($\tau_{Ly\alpha} \gg 1$) condition,[1] which is usually denoted as Case B recombination (Osterbrock 1989), $I_{H\alpha}$ in erg cm^{-2} s^{-1} sr^{-1} is given by (Valls-Gabaud 1998):

$$I_{H\alpha} = 9.41 \times 10^{-8} T_e^{-1.017} 10^{(\frac{-0.029}{T_e})} \text{EM} \quad (6)$$

where T_e is the electron temperature in units of 10^4 K, and EM is in cm^{-6} pc. Equation (6) is more than 1 per cent precise for electron temperatures of 5000–20 000 K. Oster (1961) presents an expression of the free–free continuum optical thickness radiated from an ionized

---

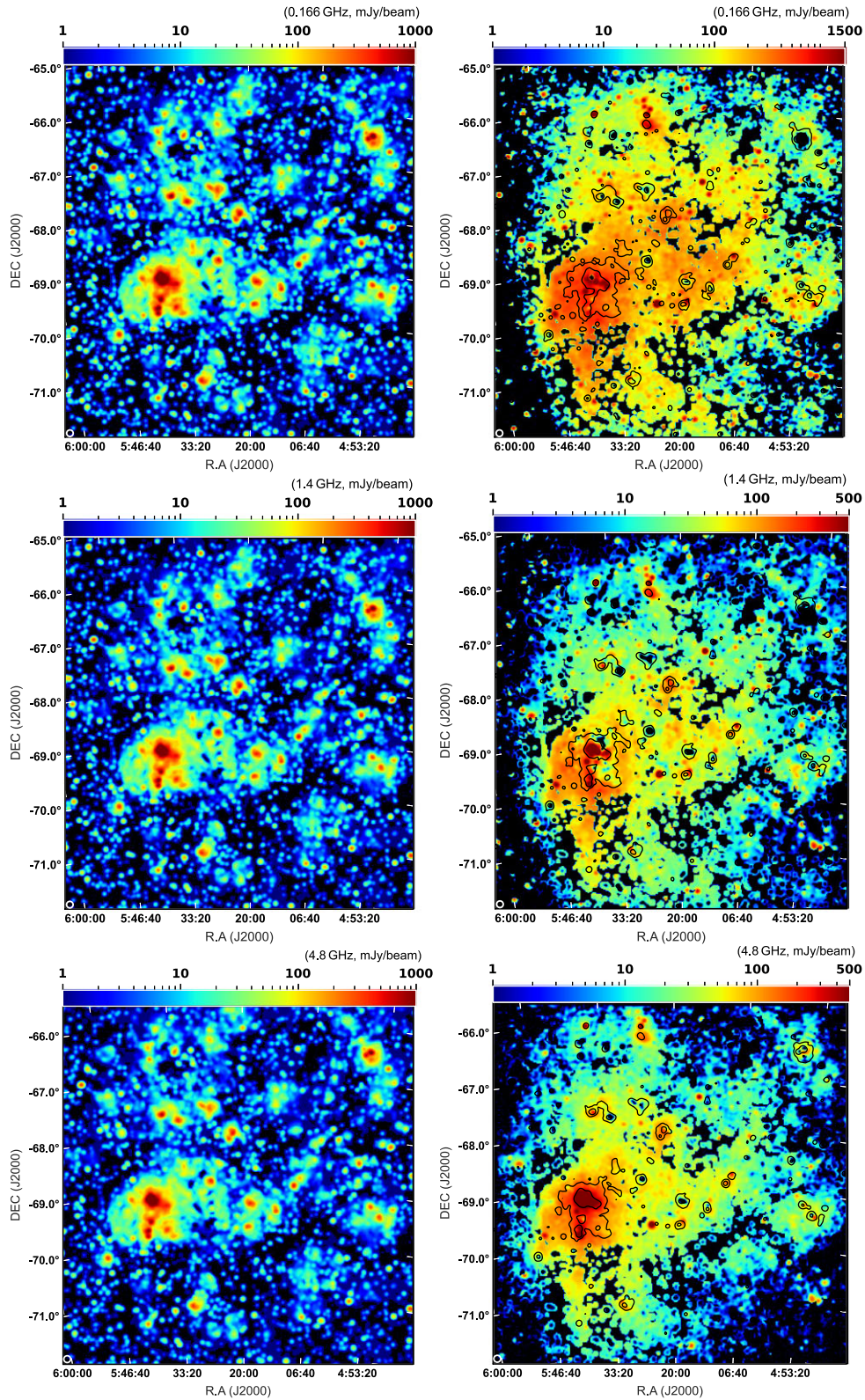[1]The optically thin condition is discussed in Section 6.5.

Figure 5. The LMC: The thermal free–free (left) and the non-thermal synchrotron (right) emission maps at 0.166 (top), 1.4 (middle), and 4.8 GHz (bottom). Colour bars show the intensities in units of mJy beam^{-1} on a log scale. The non-thermal maps are overlaid with contours of the thermal emission with levels of 40 and 100 mJy beam^{-1}. The beam size of 221 arcsec is shown in the lower left-hand corners of the maps.
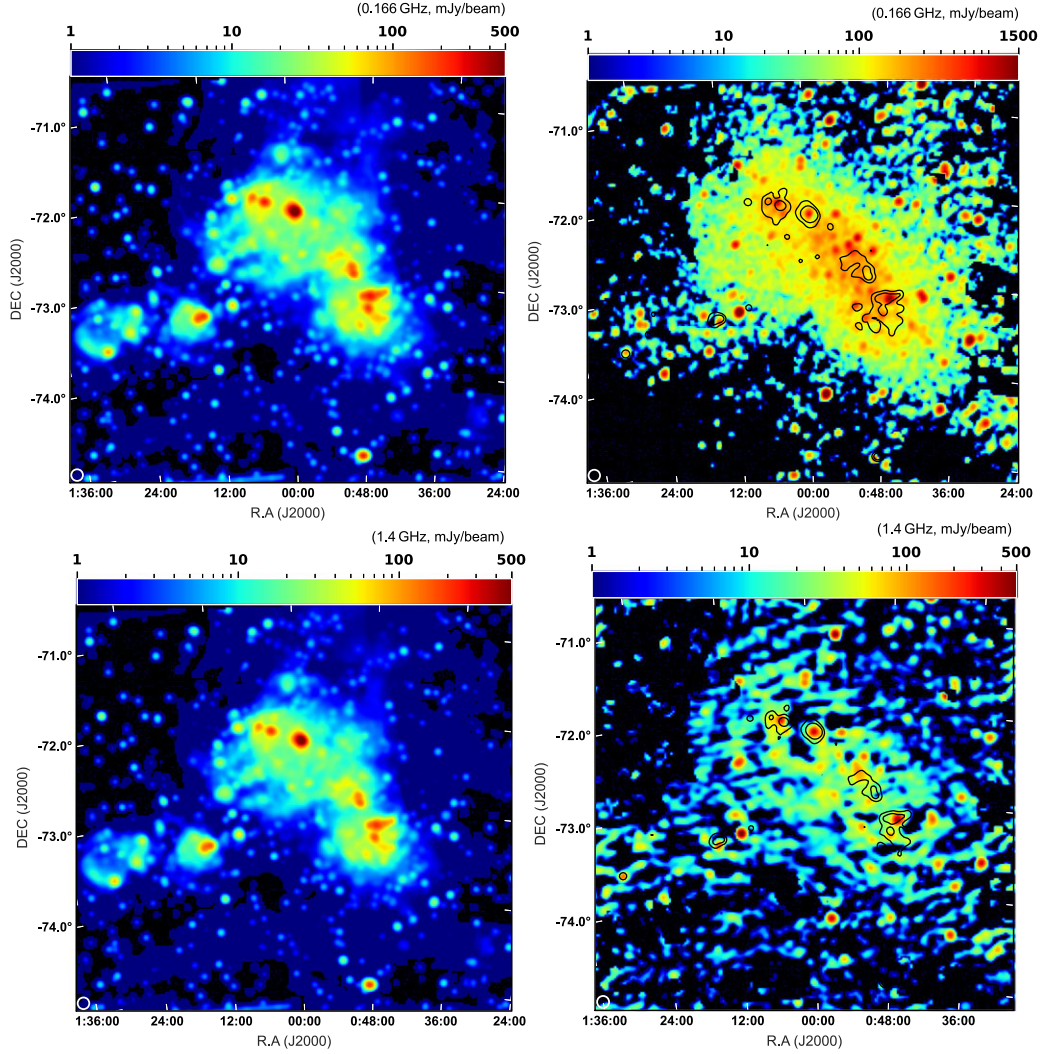
Figure 6. The SMC: The thermal free–free (left) and the non-thermal synchrotron (right) emission maps at 0.166 (top) and 1.4 GHz (bottom). Colour bars show the intensities in units of mJy beam^{-1} on a log scale. The non-thermal maps are overlaid with contours of the thermal emission with levels of 40 and 100 mJy beam^{-1}. The beam size of 235 arcsec is shown in the lower left-hand corners of the maps.

Table 6. Measured fluxes $F_{H\alpha}$ and $F_{H\beta}$ of the MUSE SNR fields and their corresponding central wavelengths (CW). Also shown are dust surface density (Σ_d), visual extinction (A_V), and fraction of dust attenuating H α emission (f_d).

Field	$CW_{H\alpha}$ (Å)	$CW_{H\beta}$ (Å)	$F_{H\alpha}$ (10^{-12} erg s^{-1} cm^{-2})	$F_{H\beta}$ (10^{-12} erg s^{-1} cm^{-2})	Σ_d (10^{-5} g cm^{-2})	A_V	f_d
LMC/N49	6567.48	4864.98	50.9 ± 2.5	11.9 ± 0.6	16.6 ± 1.2	0.9 ± 0.5	0.3 ± 0.1
LMC/SNR 0540–69.3	6568.74	4866.24	4.4 ± 0.2	0.9 ± 0.1	16.8 ± 0.1	1.2 ± 0.5	0.3 ± 0.1
SMC/1E0102–7219	6566.07	4863.57	3.3 ± 0.1	1.1 ± 0.1	6.0 ± 0.5	0.2 ± 0.1	0.2 ± 0.1

gas:

$$\tau_c = 0.082\,35 \times a\, T_e^{-1.35}\, \nu_{GHz}^{-2.1}(1 + 0.08)\, EM \qquad (7)$$

where $a \simeq 1$ and the continuum optical depth is corrected for singly ionized He atoms by the factor $(1 + 0.08)$.

The brightness temperature T_b of the radio continuum (free–free) emission in kelvins is given by:

$$T_b = T_e(1 - e^{\tau_c}). \qquad (8)$$

The brightness temperature is converted to the radio flux density (Jy beam^{-1}) using factors of 1.0, 78.2, and 919.3 for the LMC

at 0.166, 1.4, and 4.8 GHz respectively. These factors are 1.2 and 88.4 for the SMC at 0.166 and 1.4 GHz respectively. The electron temperature is the only free parameter in this conversion. Different methods of electron temperature determination (Dufour 1975; Dufour & Harlow 1977; Peck et al. 1997; Vermeij & van der Hulst 2002) indicate that $8000 < T_e < 12\,000$ K in the MCs. However, we adopt $T_e = 10^4$ K as this variation would not change the thermal emission by more than 20 per cent.

The free–free maps are presented in Figs 5 and 6 (left-hand panels) at frequencies of 0.166, 1.4, and 4.8 GHz. The strongest thermal emission is visible in the MCs' H II regions; in particular, the LMC

Table 7. The effect of background source subtraction on the integrated flux densities of the observed RC (S) and the non-thermal (S_{nt}) emission for the LMC ($R \leq 5°$) and the SMC ($R \leq 3°$).

ν (GHz)	S (Jy)	S_{nt} (Jy)
LMC		
0.166^a	1353 ± 138	1179 ± 130
0.166^b	641 ± 70	467 ± 51
1.4^a	449 ± 30	304 ± 22
1.4^b	385 ± 26	240 ± 18
1.4^c	242 ± 16	97 ± 7
4.8^a	361 ± 31	232 ± 21
4.8^b	347 ± 29	218 ± 22
4.8^c	231 ± 20	102 ± 9
SMC		
0.166^a	260 ± 35	238 ± 33
0.166^b	126 ± 17	104 ± 14
1.4^a	49.7 ± 6.3	32 ± 4
1.4^b	30.2 ± 3.9	12.5 ± 1.7
1.4^c	18.9 ± 2.5	1.2 ± 0.2

Note. a − Background sources not subtracted. b − Background sources subtracted at native resolutions (see Table 2). c − Background sources subtracted after convolution to the GLEAM resolutions.

H II region 30 Dor has a significant amount of free–free emission reaching 6 Jy beam^{-1} at 0.166 GHz. The other LMC H II regions like N11 and N44 reach 0.5 Jy beam^{-1} as well as N66 in the SMC.

4.2 Mapping synchrotron emission

The synchrotron emission maps are obtained at frequencies of 0.166, 1.4, and 4.8 GHz by subtracting the thermal map from the observed RC map (Figs 5 and 6). Strong synchrotron emission emerges from the brightest H II complex of the LMC, 30 Dor, possibly due to a strong magnetic field and/or energetic CREs in this massive star-forming region. This source is the most prominent feature of the synchrotron emission from 0.166–4.8 GHz. Extended diffuse synchrotron emission is also clearly visible around 30 Dor. At 1.4 GHz, this region is affected by observational artefacts (Hughes et al. 2007) reducing the sensitivity to detect the diffuse emission at distances about 0.6 kpc from the centre of 30 Dor in the north. In the SMC, extended synchrotron emission is found along its bar. The synchrotron emission is also strong in other H II regions that are classically considered as thermal sources, such as H II N44 and N11 of the LMC and N66 and N19 in the SMC, as indicated by contours of the thermal emission overlaid on the non-thermal maps in Figs 5 and 6. This non-thermal intensity is probably due to SNRs and strong non-thermal shocks in these young massive star clusters and associations. Similar non-thermal emission was previously shown to exist in the H II regions of M33 (Tabatabaei et al. 2007). The SNRs as an intense source of energetic CREs show a strong magnetic field as previously indicated by Klein et al. (1989). The known SNRs (Bozzetto et al. 2017; Maggi et al. 2019) are well matched with the brightest sources of our non-thermal maps.

Table 7 shows the integrated flux densities of the synchrotron and observed RC emission. Integrations were performed from the LMC centre ($5^h23^m34^s$, $-69°45'22''$)$_{J2000}$ out to a radius of $R = 5°$ and from the SMC centre ($0^h52^m44^s$, $-72°49'42''$)$_{J2000}$ out to $R = 3°$. We note that negative map pixels are neglected in these calculations. Otherwise, these pixels reduce the integrated flux density of the observed radio continuum emission by at most 30–35 per cent at 0.166 GHz in both the LMC and the SMC and at

1.4 GHz in the SMC, resulting in an artificial increase in the thermal fraction by about 15 per cent (see Section 4.3). For comparison, the integrated flux densities are reported before and after subtracting the background radio sources presented by Filipović et al. (2021) and Payne et al. (2004). These sources account for 53 per cent, 14 per cent, and 4 per cent of the total RC flux at 0.166, 1.4, and 4.8 GHz, respectively, in the LMC, indicating that they are mostly steep radio sources ($\alpha < -1.1$). However, we note that as most of these sources are behind the face of the LMC, and hence mixed with the galaxies' extended emission, the resolution at which this subtraction is performed becomes important.

Table 7 shows that the source subtraction from the 1.4 and 4.8 GHz maps results in lower galaxy integrated fluxes (or higher fluxes of background sources at this frequency leading to their flatter spectra) at the GLEAM resolutions (221 and 235 arcsec) than at their own native resolutions (≤ 40 arcsec for the LMC and 98 arcsec for the SMC; see Table 2). This indicates that subtracting the sources from the GLEAM maps at 0.166 GHz also removes a portion of the extended emission of the galaxies. Hence, studies of the spectral index at which the source-subtracted maps/fluxes at different frequencies are used is actually sensitive to the resolution at which the subtraction is performed (see Section 5).

4.3 Thermal fraction

The thermal faction f_{th} maps are obtained by dividing the thermal emission by the observed RC at each frequency (Fig. 7). The prominent regions emitting strong free–free emission are H II regions with a median thermal fraction of $f_{th}^{0.166\,GHz} = (49 \pm 9)$ for the LMC and $f_{th}^{0.166\,GHz} = (32 \pm 5)$ per cent for the SMC at 0.166 GHz. The H II regions have a higher thermal fraction at 1.4 GHz with a median $f_{th}^{1.4\,GHz} = (75 \pm 9)$ per cent for the LMC and $f_{th}^{1.4\,GHz} = (79 \pm 10)$ per cent for the SMC. Tables 4 and 5 list $f_{th}^{0.166\,GHz}$ and $f_{th}^{1.4\,GHz}$ for the individual H II regions.

The global thermal fraction obtained above the 5σ rms level of the thermal emission is $f_{th}^{1.4\,GHz} = (30 \pm 4)$ per cent in the LMC and slightly higher (35 ± 7) per cent in the SMC at 1.4 GHz. In both galaxies, the thermal fraction at 0.166 GHz is less than 15 per cent. The lower thermal fraction at lower frequencies is expected due to a faster increase of the synchrotron emission than the thermal emission. The MCs' global thermal fractions are higher compared with those of spiral galaxies such as M33 ($f_{th} \sim 18$ per cent) and NGC 6946 ($f_{th} \sim 7$ per cent) at 1.4 GHz (Tabatabaei et al. 2008, 2013a). However, they are lower than those estimated using the classical separation method, i.e. using a fixed spectral index, in the same galaxies (e.g. $f_{th}^{1.4\,GHz} \simeq 55$ per cent in the LMC assuming $\alpha_n = -0.84$, Klein et al. 1989). This assumption in particular leads to excess thermal emission in H II regions. Previously, Klein et al. (1989) indicated that the 30 Dor complex is mostly thermal (at least at 1.4 GHz); however, we find strong non-thermal emission as well.

5 NON-THERMAL SPECTRAL INDEX

The TRT separation technique used is independent of the synchrotron spectrum and free from any related assumption. Its products at several frequencies can be used to investigate variations in the non-thermal radio spectral index. The synchrotron emission is characterized by a power-law spectrum with an index α_n, $S_n \simeq \nu^{\alpha_n}$. We map α_n of the MCs between 0.166 and 1.4 GHz using the non-thermal maps at the corresponding frequencies. These maps, as well as those of the observed spectral index α, $S \simeq \nu^\alpha$, are derived only for pixels with intensities higher than 5σ rms noise in the MCs. Both the LMC
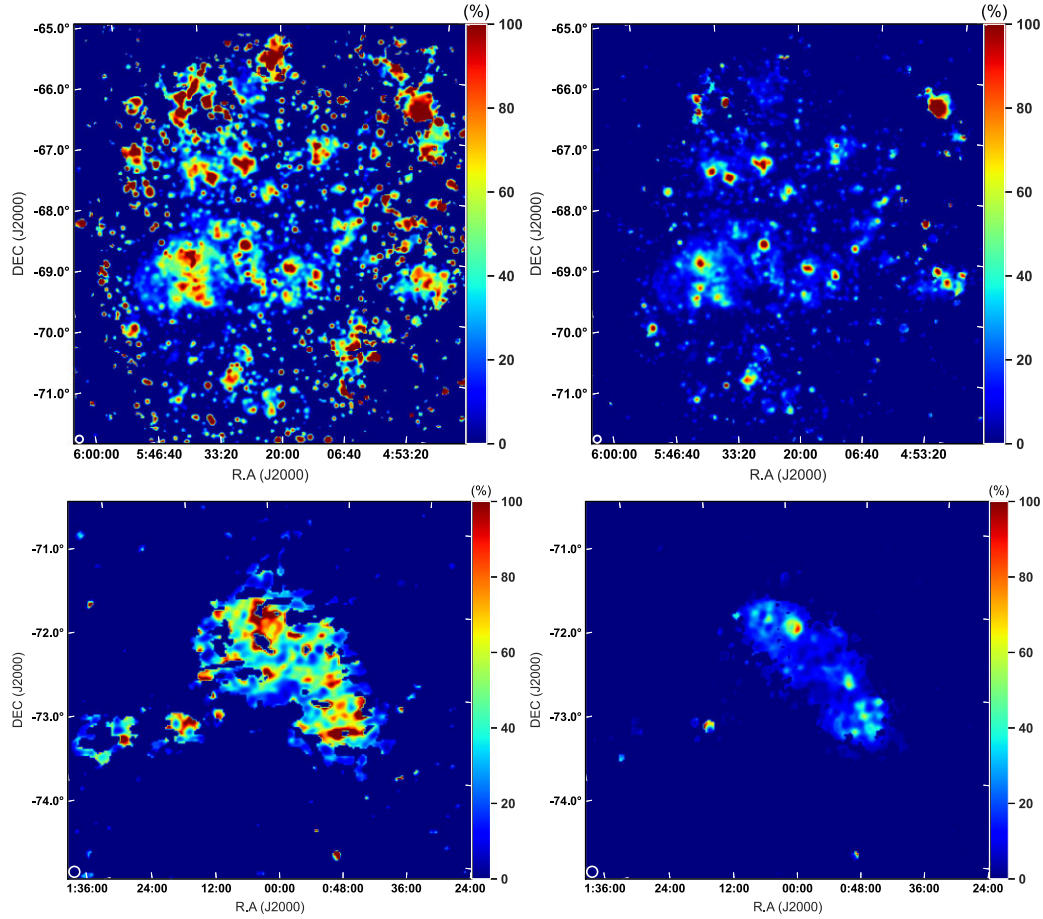
Figure 7. Maps of the thermal fraction for the LMC (top) and the SMC (bottom) at 0.166 (left) and 1.4 GHz (right). Colour bars show the fractions in percentage. The beam sizes of 221 arcsec (for the LMC) and 235 arcsec (for the SMC) are shown in the lower left-hand corners of the maps.

and the SMC show regions of steep spectrum ($\alpha < -0.8$, dark-blue regions in Figs 8 and 9), which mostly belong to diffuse parts of the ISM. In massive star-forming regions, the spectrum, even that of pure synchrotron emission, is relatively flat ($-0.7 \lesssim \alpha_n \lesssim -0.4$), indicating the presence of high-energy CREs in these regions. The flattest spectrum is found in the giant H II complex 30 Dor in the LMC.

To obtain an average value of the spectral index, it is essential first to subtract the background radio sources at different frequencies. As discussed in Section 4.2, the final result can change depending on the resolution at which that subtraction is performed. Hence, to keep the residual structures consistent at different frequencies, we have to subtract the sources at the same resolution as the GLEAM data at 0.166 GHz. In other words, at 1.4 GHz, the maps are first convolved to the GLEAM resolution then subtracted for the sources. We note that this way, the spectral index measurement is accurate, but the ISM regions with a background source behind are excluded, which is unavoidable due to the large beam of the GLEAM data.

Fig. 10 shows a histogram of α and α_n obtained using the background radio source-subtracted intensity maps at 0.166 and 1.4 GHz. We found that both α and α_n are flatter in the LMC ($\alpha = -0.58 \pm 0.10$ and $\alpha_n = -0.67 \pm 0.12$) than in the SMC ($\alpha = -0.78 \pm 0.12$ and $\alpha_n = -0.89 \pm 0.17$); this is mainly due to the presence of 30 Dor and the fact that the LMC hosts more giant H II regions with flat spectra than the SMC.

Using all multifrequency RC maps and archival data available, we further obtain α_n globally over a wider range of frequencies by modelling the integrated RC spectrum from 0.02–8.5 GHz in the LMC and 0.08–8.5 GHz in the SMC. All maps are integrated out to a radius of $5°$ for the LMC and $3°$ for the SMC from their centres (see Table 1). Tables 8 and 9 summarize our integrated flux measurements[2] as well as measurements from the literature.

Assuming that the thermal emission is optically thin, the RC spectrum can be expressed as:

$$S_\nu = S_\nu^{th} + S_\nu^{nt} = A_1 \, \nu^{-0.1} + A_2 \, \nu^{\alpha_n}, \quad (9)$$

where A_1 and A_2 are constant scaling factors. To avoid dependences on the units of the frequency space, this equation can be written as:

$$S_\nu = A_1' \left(\frac{\nu}{\nu_0} \right)^{-0.1} + A_2 \, \nu_0^{\alpha_n} \left(\frac{\nu}{\nu_0} \right)^{\alpha_n}, \quad (10)$$

with $A_1' = \nu_0^{-0.1} A_1$ and ν_0 a reference frequency. Following Tabatabaei et al. (2017), we fit this model to the observed data using the Markov chain Monte Carlo (MCMC) Bayesian method as it provides robust statistical constraints on the fitting parameters α_n, A_1', and A_2. The priors and related model library are set by generating random combinations of the parameters sampled uniformly in wide

---

[2]In Tables 8 and 9, the integrations refer to the $> 3\sigma$ level of the RC maps, leading to slightly lower values than those listed in Table 7.
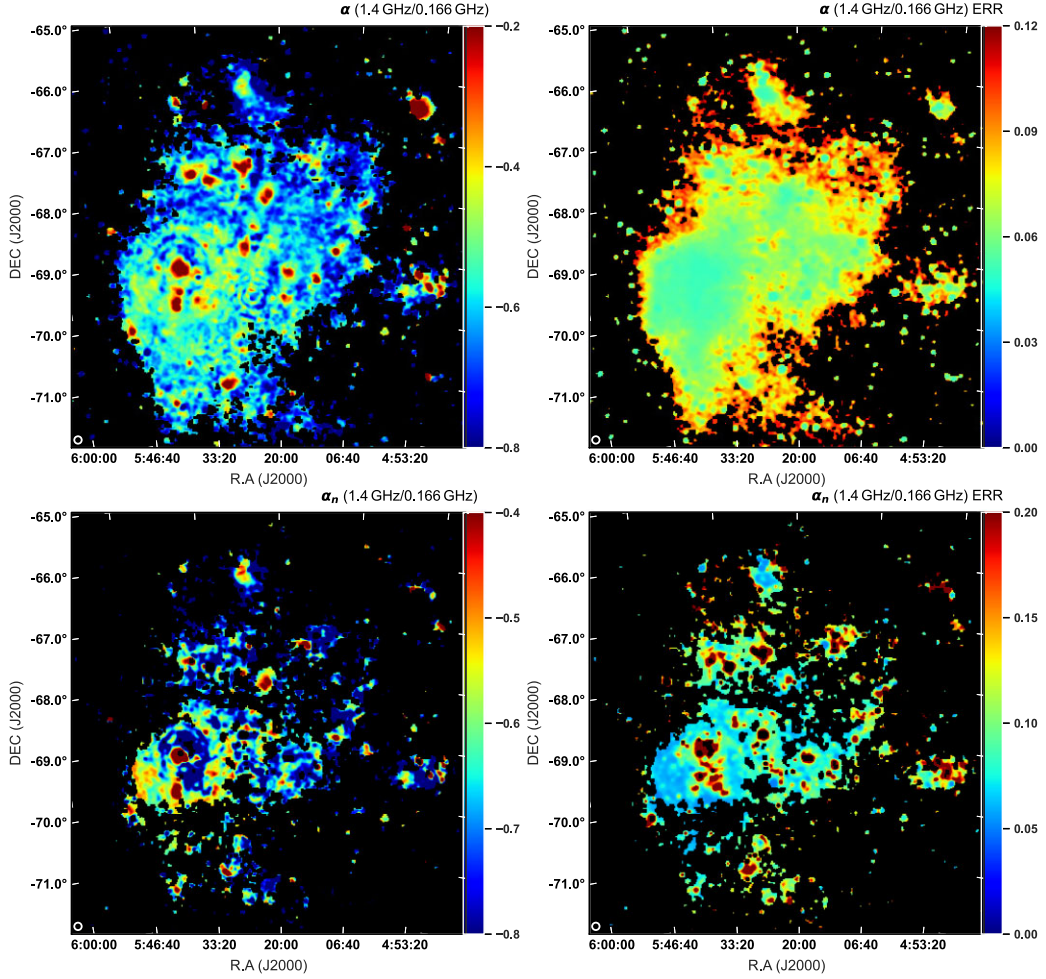
Figure 8. Maps of the spectral index (left) and its uncertainty (right) of the observed RC (α, top) and synchrotron emission (α_n, bottom) measured between 0.166 and 1.4 GHz for the LMC. The beam size of 221 arcsec is shown in the lower left-hand corners.

ranges of parameter space ($-1 < A_1'$, $A_2 < 2000$ for the LMC and $-1 < A_1'$, $A_2 < 400$ for the SMC,[3] and $0 < \alpha_n < 2.2$; Tabatabaei et al. 2017). The parameters A_1' and A_2 are set to fit the integrated flux densities in units of Jy.

Figs 11 and 12 show the resulting fit to the integrated flux densities and the posterior probability distribution function (PDF) of the parameters, respectively.

We obtain a global non-thermal spectral index $\alpha_n = -0.65 \pm 0.04$ in the LMC and -0.74 ± 0.04 in the SMC using a reference frequency of $\nu_0 = 0.166$ GHz. These results agree with the median of the α_n distribution in the maps presented above. Moreover, we find a good match with the results of For et al. (2018) studying the integrated RC SEDs. Our fitting process suggests a curved line for the LMC, which agrees with the best-fitting model suggested by For et al. (2018). The curvature shows that both the thermal and non-thermal components are indeed necessary to explain the RC spectrum in the LMC. The non-thermal emission is dominant at lower frequencies, the thermal emission at higher frequencies. In the SMC, however, the non-thermal emission dominates the RC spectrum at the selected frequency range, which also agrees with For et al. (2018).

---

[3]We note that negative values of flux density are not physically motivated but are included to assess the robustness of the final results.

6 DISCUSSION

After mapping the extinction and de-reddening the H α emission, we have presented the distribution of the thermal and non-thermal components of the radio continuum emission across the MCs. In this section, we first derive total magnetic field strength, compare the thermal and magnetic energy densities, and investigate a possible correlation between magnetic field and massive star formation. Moreover, we compare different CRE cooling mechanisms in the MCs.

6.1 Magnetic field strength

Assuming equipartition between the energy densities of the magnetic field and cosmic rays (CRs) and using synchrotron intensity (I_n), the total magnetic field strength can be derived (e.g. Beck & Krause 2005; Tabatabaei et al. 2008):

$$B_{\text{tot}} = C(\alpha_n, K, L) \, I_n^{\frac{1}{\alpha_n+3}} \quad (11)$$

where C is the function of the non-thermal spectral index, K the ratio between the number densities of cosmic ray protons and electrons, and L is the synchrotron emitting medium's path-length. Maps of the total magnetic field strength are shown in Fig. 13 assuming a fixed $K = 100$ (Beck & Krause 2005).
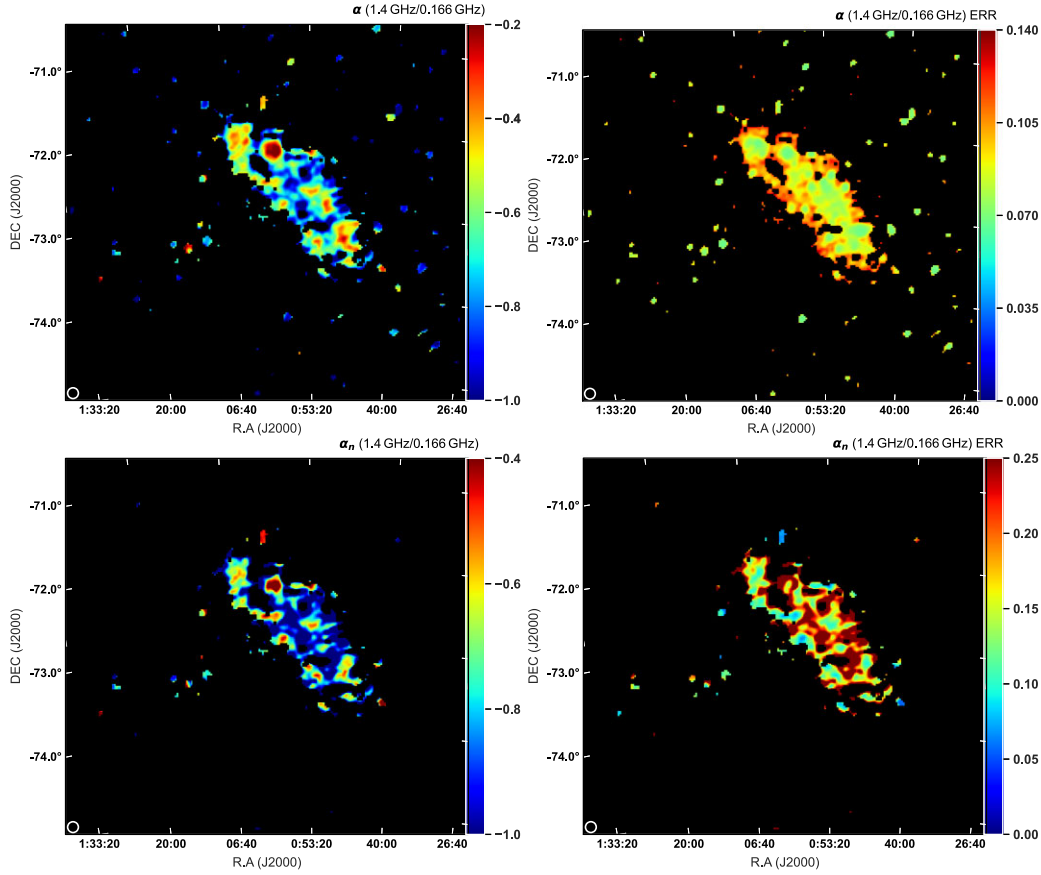
Figure 9. Maps of the spectral index (left) and its uncertainty (right) of the observed RC (α, top) and synchrotron emission (α_n, bottom) measured between 0.166 and 1.4 GHz for the SMC. The beam size of 235 arcsec is shown in the lower left-hand corners.
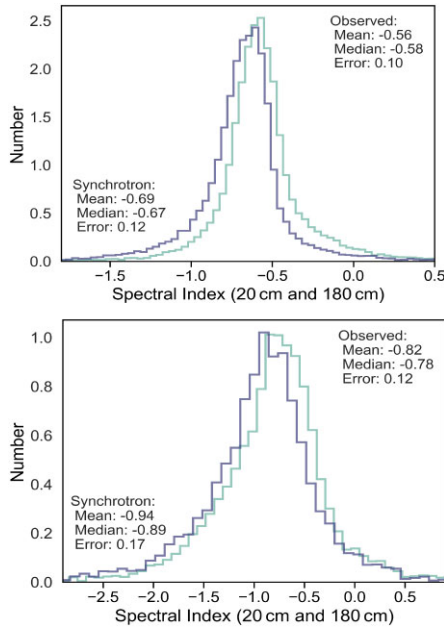

Figure 10. Histograms of the spectral index of the observed RC emission α (green) and its synchrotron component α_n (purple) measured between 0.166 and 1.4 GHz in the LMC (top) and the SMC (bottom). Vertical axes show the number of pixels in the spectral index maps corresponding to bins of equal width of α or α_n values. The intensity maps were subtracted for background radio sources before deriving the α and α_n maps.

Using our non-thermal maps, the mean non-thermal spectral index $\alpha_n = -0.67$, and a synchrotron path-length of $L = 530$ pc (Gaensler et al. 2005) in the LMC, we derive a mean total magnetic field $B_{tot} = 10.1 \pm 1.7$ μG with the errors being the uncertainties propagated in the non-thermal intensity and α_n. This is higher than the previous equipartition estimate given by Klein et al. (1989). The magnetic field is maximum in 30 Dor, $B_{tot} = 45 \pm 7$ μG, but few other H II regions such as N48B and N63A also show the presence of strong magnetic fields. We note that the synchrotron intensity measures the total magnetic field perpendicular to the line of sight. The magnetic field along the line of sight is about 4.3 μG as estimated by Gaensler et al. (2005) using the Faraday rotation measures. Our equipartition assumption agrees with Mao et al. (2012) who showed that this condition holds in the LMC using the energy density of the cosmic ray with an ordinary cosmic ray proton-to-electron ratio $K = 100$ and an upper limit of $B_{tot} = 7$ μG.

For the SMC, large uncertainties are found with measurements of L in the literature. Assuming a 1 kpc thick disc for this galaxy, $L = 1$ kpc $\times \cos(i)^{-1} = 2$ kpc, we obtain the total magnetic field strength $B_{tot} = 5.5 \pm 1.3$ μG using $\alpha_n = -0.89$, which agrees with Loiseau et al. (1987). However, adoption of a lower inclination $i = 40°$ from Stanimirovic, Staveley-Smith & Jones (2004) decreases the magnetic field strength by 10 per cent in the SMC. The total magnetic field strength is higher than that presented by Mao et al. (2008). It also appears that the magnetic field of the SMC is much more dominated by diffuse synchrotron emission than the LMC. Previous studies also show that (total) magnetic field strength in dwarf galaxies is about three times weaker than in spiral galaxies (Chyży et al. 2011).

Table 8. Integrated flux density (S_ν) and uncertainty in flux density (σ) of the LMC.

ν (MHz)	S_ν (Jy)	σ (Jy)	Reference
20	5270	1054	Shain (1959)[1]
45	2997	450	Alvarez, Aparici & May (1987)
76	1857	315.7	For et al. (2018)[1]
84	1743.3	296.4	For et al. (2018)[1]
85	3689	400	Mills (1959)[2]
92	1619.7	275.3	For et al. (2018)[1]
97	2839	600	Mills (1959)[2]
99	1511.3	256.9	For et al. (2018)[1]
107	1853.7	315.1	For et al. (2018)[1]
115	1646.4	279.9	For et al. (2018)[1]
123	1614.1	274.4	For et al. (2018)[1]
130	1580.3	268.6	For et al. (2018)[1]
143	1670.3	284	For et al. (2018)[1]
150	1406	239	For et al. (2018)[1]
158	1267	215.4	For et al. (2018)[1]
158	1736	490	Mills (1959)[2]
166	1125.7	191.4	For et al. (2018)[1]
174	1334.2	226.8	For et al. (2018)[1]
181	1235.4	210	For et al. (2018)[1]
189	1245.9	211.8	For et al. (2018)[1]
197	1070.2	181.9	For et al. (2018)[1]
204	1247.8	212.1	For et al. (2018)[1]
212	1086	184.6	For et al. (2018)[1]
219	1033.6	175.7	For et al. (2018)[1]
227	997	169.5	For et al. (2018)[1]
408	925	30	Klein et al. (1989)
1400	478.9	30	Klein et al. (1989)[1]
1400	426.1	30	Hughes et al. (2007)[1]
2400	331	50	Filipovic et al. (1996)[1]
4750	351.5	40	Haynes et al. (1991)[1]
4750	343.5	40	Dickel et al. (2005)[1]
8550	268.3	40	Haynes et al. (1991)[1]
8550	263	40	Dickel et al. (2005)[1]

Notes. [1]Reintegrated for $R \leq 5°$.
[2]Revised by Klein et al. (1989).

Table 9. Integrated flux density (S_ν) and uncertainty in flux density (σ) of the SMC.

ν (MHz)	S_ν (Jy)	σ (Jy)	Reference
76	356.2	96.2	For et al. (2018)[1]
84	272.5	73.6	For et al. (2018)[1]
85.5	460	200	Mills (1959)[2]
92	233	62.9	For et al. (2018)[1]
99	239.6	64.7	For et al. (2018)[1]
107	330.2	89.1	For et al. (2018)[1]
115	246.5	66.5	For et al. (2018)[1]
123	240.4	64.9	For et al. (2018)[1]
130	228.4	61.7	For et al. (2018)[1]
143	304.7	82.3	For et al. (2018)[1]
150	250.3	67.6	For et al. (2018)[1]
158	245	66.2	For et al. (2018)[1]
166	198.8	53.7	For et al. (2018)[1]
174	352.1	95.1	For et al. (2018)[1]
181	275.8	74.5	For et al. (2018)[1]
189	249.6	67.4	For et al. (2018)[1]
197	240	64.8	For et al. (2018)[1]
204	283.6	76.6	For et al. (2018)[1]
212	223.4	60.3	For et al. (2018)[1]
219	216.7	58.5	For et al. (2018)[1]
227	208.1	56.2	For et al. (2018)[1]
408	133	10	Loiseau et al. (1987)
1400	35	6	Wong et al. (2011a)[1]
1400	41.2	6	Haynes et al. (1991)[1]
2450	25.6	7	Haynes et al. (1991)[1]
4750	18.1	5	Haynes et al. (1991)[1]
8550	12.4	5	Haynes et al. (1991)[1]

Notes. [1]Reintegrated for $R \leq 3°$.
[2]Revised by Loiseau et al. (1987).

We note that assuming a revised minimum energy formula following Beck & Krause (2005) does not change the total magnetic field strength significantly (less than 5 per cent). The total magnetic field strength obtained from TRT's non-thermal emission is higher than using 'classical' non-thermal maps. Using a fixed radio spectral index for separation in all regions (including H II regions) causes lower non-thermal emission and hence underestimates the magnetic field strength.

6.2 Thermal versus magnetic energy density

The corrected Hα emission or the thermal free–free emission is an ideal tracer of the density of thermal electrons n_e (Condon 1992). The emission measure, EM, of the thermal emission is related to n_e as $EM = \int n_e^2 . dl = \langle n_e^2 \rangle L$, with L the line-of-sight path-length of the ionized medium.[4] The volume-averaged electron density along the line of sight is given by $\langle n_e \rangle = \sqrt{f \langle n_e^2 \rangle}$, with f the volume filling factor describing the fluctuations in n_e ($f \simeq 5$ per cent following Ehle & Beck 1993; Gaensler et al. 2008).

---

[4]It is assumed to be the same as that of the magneto-ionic medium (Section 6.1).

A large variation in $\langle n_e \rangle$ is obtained in the LMC ranging from $0.01 \, \text{cm}^{-3}$ in weak diffuse regions to higher than $1 \, \text{cm}^{-3}$ in dense areas of 30 Dor with a mean of $0.045 \, \text{cm}^{-3}$ (median $0.033 \, \text{cm}^{-3}$). Considering only 30 Dor, we obtain $\langle n_e \rangle = 0.30 \pm 0.01$ on average. Assuming $L = 530 \, \text{pc}$, the mean volume-averaged electron density increases to $0.062 \, \text{cm}^{-3}$, which agrees with the distribution modelling of Yao, Manchester & Wang (2017).

For the SMC, we obtain $\langle n_e \rangle = 0.020 \pm 0.019 \, \text{cm}^{-3}$ with the error being the standard deviation. This agrees with Mao et al. (2008) deriving a mean electron density of $0.039 \, \text{cm}^{-3}$ using the pulsar dispersion measure technique.

To address the energy balance in the magneto-ionic ISM of the MCs, the thermal energy density ($E_{th} = \frac{3}{2} \langle n_e \rangle k T_e$) is compared with the magnetic energy density ($E_B = B^2/8\pi$) for the warm ionized gas $T_e \simeq 10^4$ K. The energy density of the hot ionized gas with $T_e \simeq 10^6$ K and an electron density of $\simeq 0.01 \langle n_e \rangle$ is about the same order of magnitude as the warm ionized gas energy density assuming pressure equilibrium between the warm and hot ionized gas (e.g. Ferrari 1998). On average, the resulting magnetic energy density is larger than the thermal energy density by about one order of magnitude in both the LMC and the SMC. This means that the ionized ISM is a low-beta plasma ($\beta \equiv E_{th}/E_B < 1$) in these galaxies. In other words, the ionized ISM is magnetically confined to electron densities of $\langle n_e \rangle = 0.06 \pm 0.01$ in the LMC and $\langle n_e \rangle = 0.020 \pm 0.019$ in the SMC. Moreover, the total non-thermal pressure inserted from both CREs and magnetic fields (which is twice the magnetic pressure in the case of equipartition) dominates the thermal pressure in the ionized phase of the ISM. We summarize the magneto-ionic plasma physical properties of the MCs in Table 10.
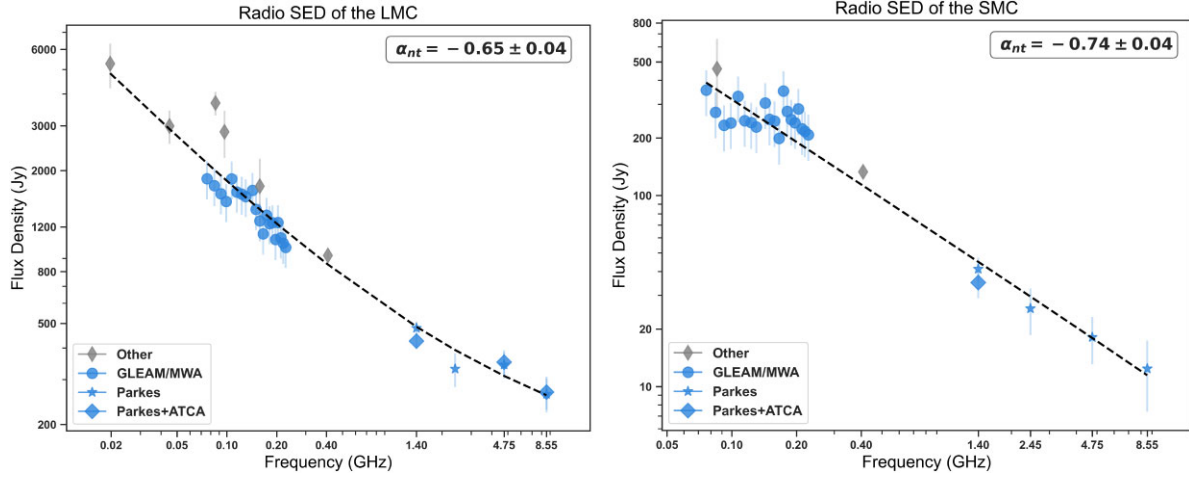
Figure 11. The radio continuum spectrum from about 0.02–8.5 GHz for the LMC (left) and the SMC (right).
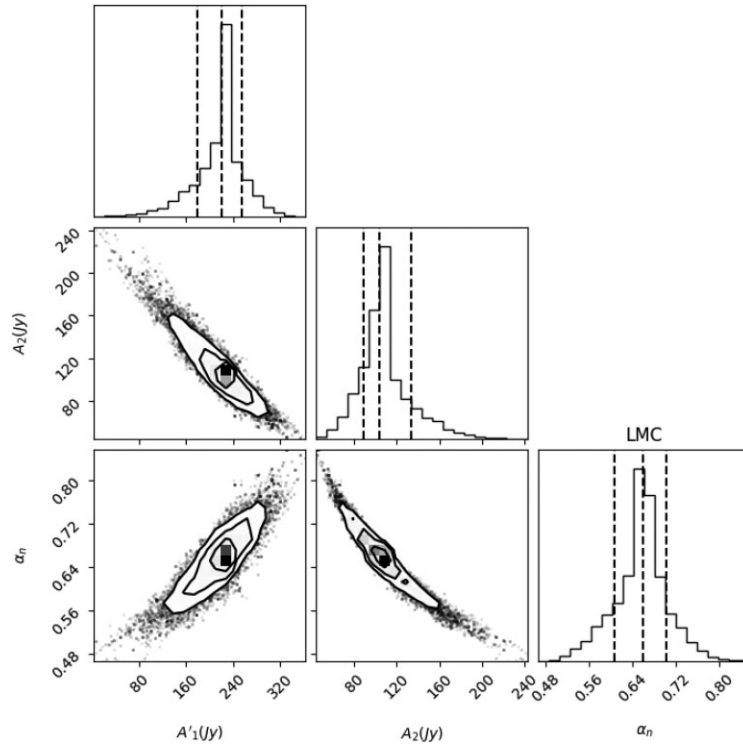

Figure 12. Bayesian corner plots for the parameters A'_1 and A_2 in equation (10) showing the posterior PDFs and their 0.16, 0.5, and 0.86 percentiles for the LMC. The uncertainty contours show that the posteriors have the highest probability of occurring within the confidence intervals indicated.

6.3 Magnetic field–star-formation rate correlation

Studies show that the magnetic field scales with the recent SFR globally in galaxies following a power-law index of about $\gamma = 0.3$ (e.g. Chyży et al. 2011; Heesen et al. 2014; Tabatabaei et al. 2017). This is linked to the amplification of the magnetic field in star-forming regions (Gressel et al. 2008; Siejkowski, Soida & Chyży 2018). However, deviations are found on local scales (e.g. Chyży 2008; Tabatabaei et al. 2013a). It is hence important to dissect the role of the diffuse ISM and spatial resolution in these studies. Thanks to their proximity, the MCs are ideal for testing this correlation at

different resolutions down to ∼50 pc. It is shown that the 70 μm infrared emission can well trace the recent star formation (over the last 100 Myr) in the MCs via the following relation (Lawton et al. 2010), which is calibrated for the H II regions in the MC:

$$\left(\frac{\mathrm{SFR}_{70\,\mu m}}{\mathrm{M}_\odot\,\mathrm{yr}^{-1}}\right) = 9.7 \times 10^{-44} \left(\frac{L_{70\,\mu m}}{\mathrm{erg\,s}^{-1}}\right). \tag{12}$$

We investigate the *B*–SFR correlation by separating the diffuse ISM from star-forming regions at different resolutions. Using $U_{\min}$ maps from Chastenet et al. (2019), we consider star-forming regions
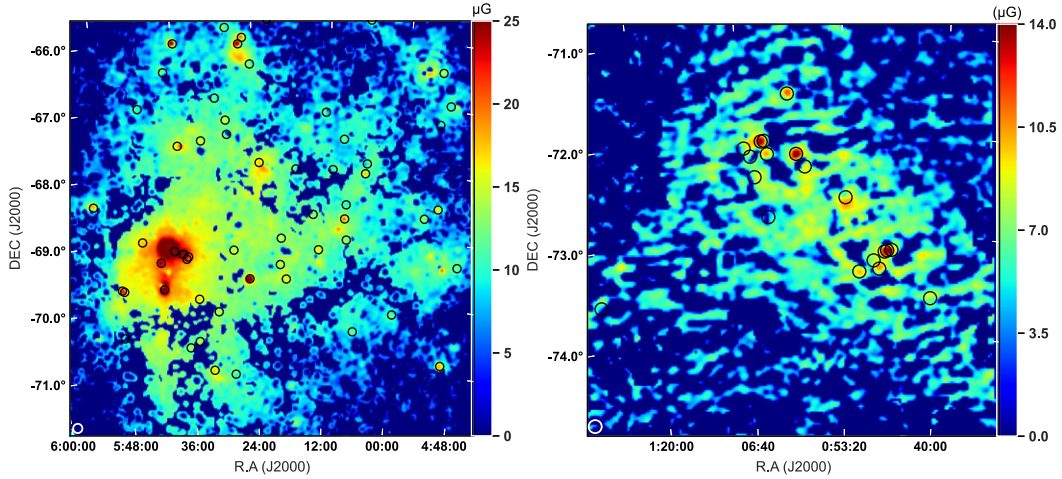
Figure 13. Total magnetic field strength of the LMC (left) and the SMC (right) derived using the background source-subtracted non-thermal intensity maps at 4.8 GHz in the LMC and at 1.4 GHz in the SMC. Colour bars show the field strength in units of μG. The beam sizes of 221 arcsec (for the LMC) and 235 arcsec (for the SMC) are indicated in the lower left-hand corners. Black circles show the position of confirmed SNRs in the LMC and the SMC (Bozzetto et al. 2017; Maggi et al. 2019).

Table 10. Mean physical properties of the magneto-ionic plasma in the MCs.

Object	B_{tot} (μG)	$\langle n_e \rangle$ (cm^{-3})	β
LMC	10.1 ± 1.7	0.06 ± 0.01	0.06 ± 0.01
SMC	5.5 ± 1.3	0.020 ± 0.019	0.06 ± 0.06

in the LMC ($U_{min} > 0.4$) and the SMC ($U_{min} > 0.5$). The correlation between magnetic field strength and 70 μm SFR is obtained through a beam-independent spacing, yielding a Pearson correlation coefficient of $r \sim 0.6$ in the LMC and the SMC. B versus SFR can best be explained by a power-law relation with an index γ fitted using the bisector OLS (Isobe et al. 1990) regression (Table 11). Fig. 14 presents the correlation of B with SFR at a spatial resolution of 53 pc for the LMC and 71 pc for the SMC.

We find that B and SFR traced by the 70 μm are correlated in the SF regions at all selected resolutions. In the LMC, the power-law exponent agrees with the theoretical turbulent amplification value (Schleicher & Beck 2013). However, in the SMC, it is slightly lower at the original resolution. As expected, no correlation holds in the diffuse ISM at the native resolution. However, it is interesting to note that this correlation is increased at lower resolutions due to mixing with the SF regions. The obtained exponents of $\gamma_{LMC} = 0.24 \pm 0.01$ and $\gamma_{SMC} = 0.20 \pm 0.01$ are in excellent agreement with global studies of Magellanic-type galaxies with slope $\gamma = 0.25 \pm 0.02$ given by Jurusik et al. (2014). This experiment shows that, in local studies, the power-law exponent can become flatter than the theoretical value because of contamination by the diffuse ISM.

6.4 Cooling of cosmic ray electrons

The power-law energy distribution of CRE, $dN/dE \propto E^{-\beta}$, where β is related to the observed spectral index with $\alpha = -(2\beta - 1)$, could change due to various energy-loss mechanisms. The non-thermal spectral index becomes steeper due to different energy losses of CRE diffusion from primary sources (e.g. H II regions). In order to clarify

the most effective energy-loss mechanism of CREs in H II regions, we study two well known H II regions in the MCs. We measure the radial profile of the average observed/non-thermal spectral index and thermal fraction centred on $(5^h38^m42^s, -69°06'03'')_{J2000}$ and $(0^h59^m05^s, -72°10'41'')_{J2000}$ in the 30 Dor and N66 H II complexes respectively using beam-independent rings of 7.2 arcmin radius in 30 Dor and 3.91 arcmin in N66. Fig. 15 shows the radial profile of the spectral index and thermal fraction from the centre of 30 Dor and N66. The spectral index profile of 30 Dor starts with very flat spectrum, $\alpha \sim 0$, in the centre but it drops rapidly moving away from the centre. At a distance of $R = 0.3$ kpc, α_n reaches a steep value (~ -0.85) and again flattens to about the average galaxy value. The flattening of the synchrotron spectrum around $R = 0.5$ kpc is most likely due to the ring-like artefact in the observed RC map at 1.4 GHz (Hughes 2011), which also leads to an artificially higher thermal fraction.

The spectral index of 30 Dor starts to fall off after $R > 0.5$ kpc due to the diffusion of CREs, but it again has two slight flattening and higher thermal fractions around $R \sim 1$ and ~ 1.4 kpc. These can be interpreted as reacceleration of CREs due to feedback and shock waves from the two nearby H II regions, N144 and N59. Overall, the 30 Dor radio spectral index should decrease slightly to the galaxy average value $\alpha = -0.64$ at a scale of $R \sim 2$ kpc. Beyond $R > 2$ kpc, the non-thermal spectral index $\alpha_n \sim -0.85$, never attaining the characteristic values of CRE synchrotron losses (i.e. $\alpha_n < -1$, Biermann & Strom 1993). Similar to 30 Dor, the N66 H II complex of the SMC also shows flat values of $\alpha = -0.1$ in the core ($R < 0.1$ kpc). The non-thermal spectral index α_n decreases to steeper values of $\alpha_n < -1$ for $R < 0.3$ kpc of N66. Such a steep α_n could be interpreted as CRE energy loss due to the synchrotron loss mechanism. However, the measurement suffers from large uncertainties due to the low sensitivity of the radio continuum data at 1.4 GHz. After $R > 0.3$ kpc, the observed spectral index increases to the mean value of the galaxy, and α_n does not reach steeper values than < -1, indicating that the synchrotron energy-loss mechanism is not an efficient cooling mechanism in N66 either. In order to assess different CRE cooling processes in the cores of these H II regions ($R < 0.2$ kpc), we estimate their cooling time-scales using the equations presented in Lacki,

Table 11. Correlation between the magnetic field strength and SFR in different radiation-field regimes (SF, ISRF) at different linear resolutions.

Y	γ^{total}	$r_{\text{p}}^{\text{total}}$	$t(n)^{\text{total}}$	γ^{SF}	r_{p}^{SF}	$t(n)^{\text{SF}}$	γ^{ISRF}	$r_{\text{p}}^{\text{ISRF}}$	$t(n)^{\text{ISRF}}$
LMC									
B (53 pc)	0.24 ± 0.01	0.61 ± 0.02	159.70(2166)	0.31 ± 0.01	0.67 ± 0.03	116.83(843)	–	0.39 ± 0.03	177.11(1281)
B (150 pc)	0.28 ± 0.01	0.57 ± 0.04	51.95(355)	0.29 ± 0.03	0.56 ± 0.08	42.07(120)	0.30 ± 0.02	0.49 ± 0.06	60.16(235)
B (300 pc)	0.31 ± 0.02	0.78 ± 0.08	22.59(63)	0.31 ± 0.04	0.70 ± 0.15	23.28(26)	0.30 ± 0.05	0.50 ± 0.15	25.36(37)
SMC									
B (71 pc)	0.20 ± 0.01	0.62 ± 0.04	65.18(328)	0.40 ± 0.04	0.64 ± 0.09	32.96(82)	–	0.38 ± 0.06	70.49(246)
B (150 pc)	0.24 ± 0.01	0.59 ± 0.07	38.53(156)	0.43 ± 0.11	0.53 ± 0.21	20.07(19)	0.28 ± 0.03	0.51 ± 0.08	41.46(132)

Note. The linear fit obtained on a logarithmic scale (Log $Y = \gamma$ Log X) using a bisector least-squares fit.

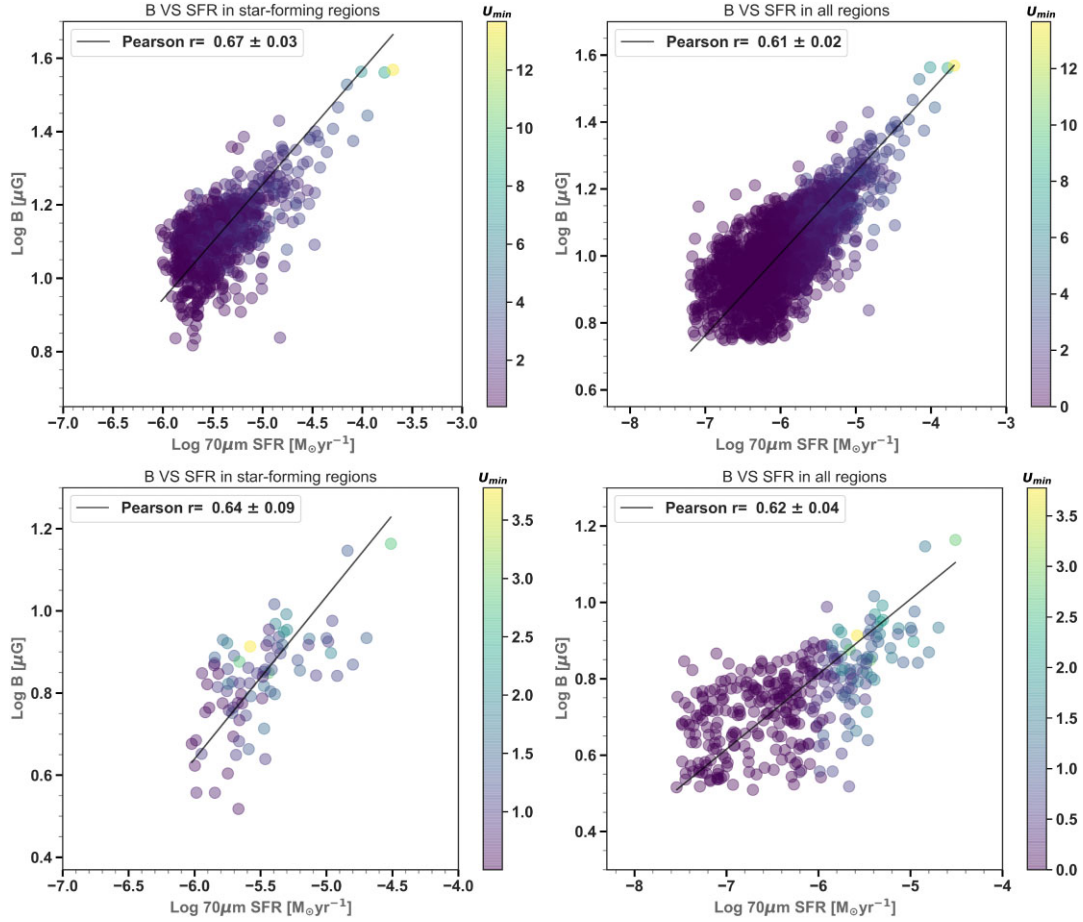**Figure 14.** Correlation between the total magnetic field strength B and the 70 μm emission as an SFR tracer for the LMC (top) and the SMC (bottom) in star-forming regions (left) as well as all regions above the 3σ rms level (right). The solid line shows the bisector fit and the bars indicate U_{min} in units of $U_{\odot}$.

Thompson & Quataert (2010):

$$\left(\frac{\tau_{\text{syn}}}{\text{yr}}\right) \approx 4.5 \times 10^7 \left(\frac{B}{10\,\mu\text{G}}\right)^{-3/2} \nu_{\text{GHz}}^{-1/2}$$

$$\left(\frac{\tau_{\text{ion}}}{\text{yr}}\right) \approx 2.1 \times 10^8 \left(\frac{B}{10\,\mu\text{G}}\right)^{-1/2} \nu_{\text{GHz}}^{1/2} \left(\frac{n_{\text{eff}}}{\text{cm}^3}\right)^{-1}$$

$$\left(\frac{\tau_{\text{IC}}}{\text{yr}}\right) \approx 1.8 \times 10^8 \left(\frac{B}{10\,\mu\text{G}}\right)^{1/2} \nu_{\text{GHz}}^{-1/2} U_{\text{rad},-12}^{-1} \quad (13)$$

$$\left(\frac{\tau_{\text{brem}}}{\text{yr}}\right) \approx 3.7 \times 10^7 \left(\frac{n_{\text{eff}}}{\text{cm}^3}\right)^{-1}$$

$$\left(\frac{\tau_{\text{diff}}}{\text{yr}}\right) \approx 2.6 \times 10^7 \left(\frac{E}{3\,\text{GeV}}\right)^{-1/2},$$

where the effective ISM number density experienced by CRs is

$n_{\text{eff}} = f_{\text{ISM}} < n >$ and the mean ISM number density within the CRE confinement volume $< n > = \Sigma_{\text{gas}}/2h$. We note that CRs traverse in high-density clumpy ISM that is confined by magnetic field experiences a higher $f_{\text{ISM}} > 1$ in comparison with a low-density diffuse ISM. We assume $f_{\text{ISM}} = 1$ for the MC.

However, taking higher $f_{\text{ISM}} > 1$ for the compact H II regions of the MCs decreases the cooling time-scale of bremsstrahlung and ionization losses, making them more effective cooling mechanisms for CR electrons and positrons by propagating away from H II regions. We assume a CR scale height of $h = 1$ kpc. The radiation energy density U_{rad} is obtained from Draine & Li (2007) and corrected for contributions of the cosmic microwave background (CMB) radiation energy density $U_{\text{CMB}} = 4.17 \times 10^{-13}$ erg cm^{-3} and dust-emission energy density $U_{\text{FIR}} = 5 \times 10^{-13}$ erg cm^{-3} (Draine 2011; Tabatabaei et al. 2013a). In order to determine the diffusion time-scale, the most
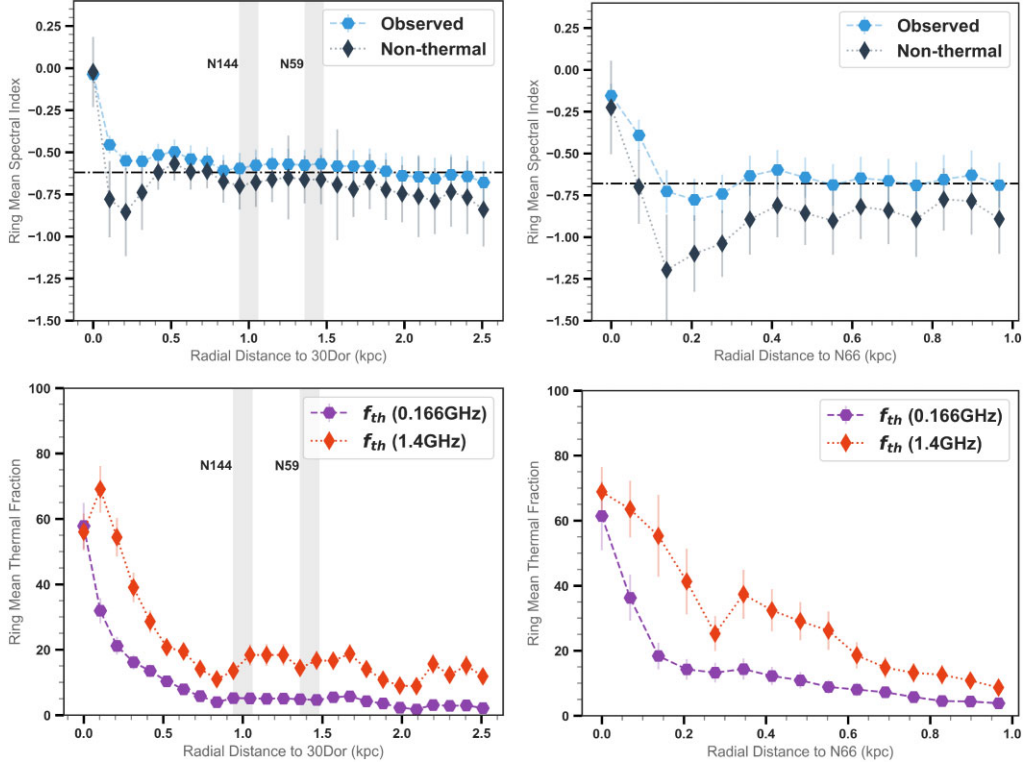
Figure 15. Radial profiles of the spectral index (top) and thermal fraction (bottom) in 30 Dor (left) and N66 (right). The dashed horizontal lines in the spectral index profiles indicate the average galaxy values. The vertical grey bands show the position of 30 Dor's neighbouring H II regions, N144 and N59.

energetic CR electrons emit at a critical frequency ν_c obtained from Murphy et al. (2012):

$$\left(\frac{E}{\text{GeV}}\right) = 8.8 \left(\frac{\nu_c}{\text{GHz}}\right)^{1/2} \left(\frac{B}{\mu\text{G}}\right)^{-1/2}. \tag{14}$$

Out to a radius of 200 pc from 30 Dor's central point, a total magnetic field strength map yields an average $B_{\text{tot}} = 26.43 \,\mu\text{G}$ and corresponding CR electron energy $\sim$3.8 GeV at 4.8 GHz. We found the average number density of the ISM experienced by the CRs is $n_{\text{eff}} \sim 0.94\,\text{cm}^{-3}$ and the average total radiation energy density $U_{\text{rad}} = 5.06\,U_{\odot}$ in 30 Dor. These estimates suggest that synchrotron escape is the dominant cosmic ray loss mechanism in 30 Dor's core, $\tau_{\text{syn}} \sim 4.7\,\text{Myr}$, and there is a strong competition between the inverse Compton cooling time-scale $\tau_{\text{IC}} \sim 26.3\,\text{Myr}$ and diffuse cooling $\tau_{\text{diff}} \sim 23.2\,\text{Myr}$ for CRs, while ionization cooling has a smaller cooling effect on CRs with a characteristic time-scale $\tau_{\text{ion}} \sim 300.8\,\text{Myr}$.

Integrating out to a radius of 100 pc from the SMC N66 complex, we found a mean $B_{\text{tot}} = 8.50\,\mu\text{G}$, CR electron energy $\sim$3.5 GeV at 1.4 GHz, and $n_{\text{eff}} \sim 0.73\,\text{cm}^{-3}$. Diffuse cooling is the most effective cooling mechanism with $\tau_{\text{diff}} \sim 23.8\,\text{Myr}$ for CRs in this region. Furthermore, it shows a strong competition between synchrotron escape, $\tau_{\text{syn}} \sim 48.5\,\text{Myr}$, and inverse Compton cooling, $\tau_{\text{diff}} \sim 45.7\,\text{Myr}$. Although ionization loss is the weakest cooling mechanism in N66, including the contribution of H_2 in the total gas surface density will decrease its cooling time-scale.

6.5 Recombination scenario

Determining extinction and free–free emission depends on the optical depth of Lyman continuum photons and whether the optically thick condition known as Case B recombination or the optically thin scenario known as case A recombination is assumed. Although the theoretical Balmer decrement ratio $j_{\text{H}\alpha}/j_{\text{H}\beta} = 2.86$ is almost the same for both scenarios under the assumption of $T_e = 10\,000\,\text{K}$ (Osterbrock 1989), the variation of EM is significant depending on the electron density as well as the optical depth of Lyman continuum photons (Valls-Gabaud 1998). Pellegrini et al. (2012) estimated that the escape fraction of Lyman continuum photons is at least $f_{\text{esc}} = 0.42$ and 0.40 in the H II regions of the LMC and SMC, respectively. Similar results were obtained by Kennicutt et al. (1995), i.e. $f_{\text{esc}} = 0.51$, based on diffuse to total Hα emission flux for the LMC (Oey & Kennicutt 1997). Adopting case A recombination increases the thermal emission flux by about 49–51 per cent for both the LMC and the SMC at 0.166 and 1.4 GHz. Consequently, the global magnetic field strength decreases by about 16 per cent.

7 CONCLUSION

Using multifrequency observations in the radio, FIR, and optical domains, we have presented the most precise picture of the distribution of the thermal and non-thermal RC emission in the MCs ever without use of any assumption about the synchrotron spectral index or extinction. The highly resolved and sensitive *Spitzer* and *Herschel* observations have allowed mapping of dust mass in galaxies in general. However, using these maps to determine extinction needs a priori assumptions about the distribution of ionized gas and dust along the line of sight. Combining the dust-mass maps with data for the Balmer decrements, we have introduced a new method

to determine the true fraction of dust that actually attenuates H α emission along the line of sight, f_{d}. This fraction is determined in the MCs for the first time in both H II regions and more diffuse regions in the ISM using the MUSE IFU observations. We have also presented a calibration relation to map f_{d} based on its anticorrelation with the neutral gas surface density. Using the de-reddened H α emission, we have derived the free–free emission at 0.166, 1.4, and 4.8 GHz and obtained maps of the non-thermal emission and the pure synchrotron spectral index in the MCs. The latter two maps allowed us to map the strength of the total magnetic field at a spatial resolution of $\sim$3.7 arcmin in the LMC and $\sim$3.9 arcmin in the SMC. Our results are summarized as follows.

(i) The dust optical depth τ_{dust} is optically thin ($\tau_{\mathrm{dust}} < 1$) to the H α photons in the MCs' diffuse ISM, whereas the total dust-mass surface density indicates that τ_{dust} ranges from 2–5 in the H II regions of the MCs. Only a fraction of this dust mass plays a role in the attenuation of optical waves.

(ii) f_{d} is lower in dense star-forming regions ($\sim$0.1) than in the more diffuse ISM ($>$0.2). Based on the anticorrelation between f_{d} and total gas surface density, we find that the mean f_{d} over the entire LMC is about 0.3, which agrees with the Milky Way value.

(iii) The non-thermal fraction is significant at 0.166 GHz with an average value of 80–90 per cent in the diffuse ISM of these galaxies and in massive star-forming regions such as N157. Supernova remnants contribute the most to our 0.166 GHz non-thermal emission map with an average value of the non-thermal fraction $>$85 per cent. Furthermore, the thermal fraction at 1.4 GHz is estimated to be $f_{\mathrm{th}} = 30$ per cent in the LMC and 35 per cent in the SMC.

(iv) The synchrotron spectrum steepens from massive star-forming regions $\alpha_{\mathrm{n}} > -0.4$ to the diffuse ISM $\alpha_{\mathrm{n}} < -0.7$. This indicates energy loss and cooling of CREs as they propagate away from their birthplaces in SF regions. After injection, CREs can also experience reacceleration in complexes of SF regions, flattening their spectrum as observed in 30 Dor. Comparing different mechanisms, we find that synchrotron energy loss dominates cooling of CREs in 30 Dor's core ($R < 0.2$ kpc). Using non-thermal maps between 0.166 and 1.4 GHz, we found the median synchrotron spectral index to be $\alpha_{\mathrm{n}} = -0.67 \pm 0.12$ and $\alpha_{\mathrm{n}} = -0.89 \pm 0.17$ in the LMC and the SMC respectively. Using this synchrotron spectral index and equipartition assumption, we found an average total magnetic field strength $B_{\mathrm{tot}} \simeq 10.1$ µG in the LMC and 5.5 µG in the SMC.

(v) This study shows that the ISM is dominated by a low-beta plasma, given that the thermal energy density is smaller than the non-thermal energy density ($E_B + E_{\mathrm{CR}}$) by more than one order of magnitude.

It is worth mentioning that the present generation of interferometric radio surveys of the MCs is limited to either low sensitivity caused by instrumental artefacts (particularly at 4.8 and 1.4 GHz) or low resolution (particularly at 0.2 GHz). The limitations in sensitivity can prevent study of the physics of the low-surface-brightness ISM that constitutes a major part of low-mass and irregular galaxies such as the MCs. Designing the next generation of the RC surveys, it is important to attain a much larger dynamic range. Technically, limitations in dynamic range can be caused by instrumental artefacts or incomplete calibration of instrumental response (Braun 2013). As discussed in Sections 4.2 and 5, the resolution at which background radio sources are subtracted can affect the integrated flux density measurements as well as the spectral index analysis in the MCs. Hence, higher-resolution observations are required (particularly at low frequencies) to disentangle the ISM from the external sources more accurately. The upcoming surveys with the SKA-Low telescope

will ideally overcome this issue in the MCs. Therefore, following these observational limitations, the main contribution of this paper is in setting a methodology for the unbiased separation of thermal versus non-thermal emission for the upcoming surveys of the MCs and nearby galaxies with the SKA and its pathfinders such as ASKAP and MeerKAT.

DATA AVAILABILITY

The data underlying this article will be shared on reasonable request.

REFERENCES

Alvarez H., Aparici J., May J., 1987, A&A, 176, 25
Bacon R. et al., 2010, Proc. SPIE Conf. Ser. Vol. 7735, The MUSE second-generation VLT instrument. SPIE, Bellingham, p. 773508
Beck R., Krause M., 2005, Astron. Nachrichten, 326, 414
Biermann P. L., Strom R. G., 1993, A&A, 275, 659
Bowman J. D. et al., 2013, Publ. Astron. Soc. Australia, 30, e031
Bozzetto L. M. et al., 2017, ApJS, 230, 2
Braun R., 2013, A&A, 551, A91
Brocklehurst M., 1971, MNRAS, 153, 471
Calzetti D., Armus L., Bohlin R. C., Kinney A. L., Koornneef J., Storchi-Bergmann T., 2000, ApJ, 533, 682
Caplan J., Deharveng L., 1985, A&AS, 62, 63
Caplan J., Ye T., Deharveng L., Turtle A. J., Kennicutt R. C., 1996, A&A, 307, 403
Cardelli J. A., Clayton G. C., Mathis J. S., 1989, ApJ, 345, 245
Chastenet J. et al., 2019, ApJ, 876, 62
Chyży K. T., 2008, A&A, 482, 755
Chyży K. T., Weżgowiec M., Beck R., Bomans D. J., 2011, A&A, 529, A94
Condon J. J., 1992, ARA&A, 30, 575
Crawford E. J., Filipovic M. D., de Horta A. Y., Wong G. F., Tothill N. F. H., Draskovic D., Collier J. D., Galvin T. J., 2011, Serbian Astron. J., 183, 95
de Jong T., Klein U., Wielebinski R., Wunderlich E., 1985, A&A, 147, L6
Dickel J. R., McIntyre V. J., Gruendl R. A., Milne D. K., 2005, AJ, 129, 790
Dickel J. R., Gruendl R. A., McIntyre V. J., Amy S. W., 2010, AJ, 140, 1511
Dickinson C., Davies R. D., Davis R. J., 2003, MNRAS, 341, 369
Draine B. T., 2011, Physics of the Interstellar and Intergalactic Medium. Princeton University Press, Princeton, New Jersey
Draine B. T., Li A., 2007, ApJ, 657, 810
Dufour R. J., 1975, ApJ, 195, 315
Dufour R. J., Harlow W. V., 1977, ApJ, 216, 706
Ehle M., Beck R., 1993, A&A, 273, 45
Ferrari A., 1998, ARA&A, 36, 539
Filipovic M. D., Haynes R. F., White G. L., Jones P. A., Klein U., Wielebinski R., 1995, A&AS, 111, 311
Filipovic M. D., White G. L., Haynes R. F., Jones P. A., Meinert D., Wielebinski R., Klein U., 1996, A&AS, 120, 77
Filipovic M. D., Jones P. A., White G. L., Haynes R. F., Klein U., Wielebinski R., 1997, A&AS, 121, 321
Filipovic M. D., Haynes R. F., White G. L., Jones P. A., 1998, A&AS, 130, 421
Filipović M. D. et al., 2021, MNRAS, 507, 885
For B. Q. et al., 2018, MNRAS, 480, 2743

Gaensler B. M., Haverkorn M., Staveley-Smith L., Dickey J. M., McClure-Griffiths N. M., Dickel J. R., Wolleben M., 2005, Science, 307, 1610

Gaensler B. M., Madsen G. J., Chatterjee S., Mao S. A., 2008, Publ. Astron. Soc. Australia, 25, 184

Gordon K. D., Clayton G. C., Misselt K. A., Landolt A. U., Wolff M. J., 2003, ApJ, 594, 279

Gordon K. D. et al., 2011, AJ, 142, 102

Graczyk D. et al., 2020, ApJ, 904, 13

Gressel O., Elstner D., Ziegler U., Rüdiger G., 2008, A&A, 486, L35

Haynes R. F., Klein U., Wielebinski R., Murray J. D., 1986, A&A, 159, 22

Haynes R. F. et al., 1991, A&A, 252, 475

Heesen V., Brinks E., Leroy A. K., Heald G., Braun R., Bigiel F., Beck R., 2014, AJ, 147, 103

Helou G., Soifer B. T., Rowan-Robinson M., 1985, ApJ, 298, L7

Hughes A., 2011, PhD thesis, Swinburne Univ. Technol.

Hughes A., Wong T., Ekers R., Staveley-Smith L., Filipovic M., Maddison S., Fukui Y., Mizuno N., 2006, MNRAS, 370, 363

Hughes A., Staveley-Smith L., Kim S., Wolleben M., Filipovic M., 2007, MNRAS, 382, 543

Hurley-Walker N. et al., 2016, MNRAS, 464, 1146

Isobe T., Feigelson E. D., Akritas M. G., Babu G. J., 1990, ApJ, 364, 104

Jameson K. E. et al., 2016, ApJ, 825, 12

Joseph T. D. et al., 2019, MNRAS, 490, 1202

Jurusik W., Drzazga R. T., Jableka M., Chyży K. T., Beck R., Klein U., Weżgowiec M., 2014, A&A, 567, A134

Kennicutt R. C., Jr, Bresolin F., Bomans D. J., Bothun G. D., Thompson I. B., 1995, AJ, 109, 594

Kim S., Staveley-Smith L., Dopita M. A., Freeman K. C., Sault R. J., Kesteven M. J., McConnell D., 1998, ApJ, 503, 674

Kim S., Staveley-Smith L., Dopita M. A., Sault R. J., Freeman K. C., Lee Y., Chu Y.-H., 2003, ApJS, 148, 473

Klein U., Wielebinski R., Haynes R. F., Malin D. F., 1989, A&A, 211, 280

Klein U., Haynes R. F., Wielebinski R., Meinert D., 1993, A&A, 271, 402

Lacki B. C., Thompson T. A., Quataert E., 2010, ApJ, 717, 1

Lakićević M. et al., 2015, ApJ, 799, 50

Lawton B. et al., 2010, ApJ, 716, 453

Leroy A. K. et al., 2011, ApJ, 737, 12

Loiseau N., Klein U., Greybe A., Wielebinski R., Haynes R. F., 1987, A&A, 178, 62

Longair M. S., 2011, High Energy Astrophysics. Cambridge Univ. Press, Cambridge

Lonsdale C. J. et al., 2009, Proc. IEEE, 97, 1497

Maggi P. et al., 2019, A&A, 631, A127

Mao S. A., Gaensler B. M., Stanimirovic S., Haverkorn M., McClure-Griffiths N. M., Staveley-Smith L., Dickey J. M., 2008, ApJ, 688, 1029

Mao S. A. et al., 2012, ApJ, 759, 25

McLeod A. F., Dale J. E., Evans C. J., Ginsburg A., Kruijssen J. M. D., Pellegrini E. W., Ramsay S. K., Testi L., 2018, MNRAS, 486, 5263

Meixner M. et al., 2006, AJ, 132, 2268

Meixner M. et al., 2010, A&A, 518, L71

Meixner M. et al., 2013, AJ, 146, 62

Meixner M. et al., 2015, AJ, 149, 88

Mills B. Y., 1959, Handb. Phys., 53, 239

Murphy E. J., Porter T. A., Moskalenko I. V., Helou G., Strong A. W., 2012, ApJ, 750, 126

Oey M. S., Kennicutt R. C., Jr, 1997, MNRAS, 291, 827

Oster L., 1961, Rev. Mod. Phys., 33, 525

Osterbrock D. E., 1989, Astrophysics of Gaseous Nebulae and Active Galactic Nuclei. University Science Books, Sausalito, CA

Paredes L., Points S. D., Smith R. C., Rest A., Damke G., Zenteno A., MCELS Team, 2015, in Points S., Kunder A., eds, ASP Conf. Ser. Vol. 491, Fifty Years of Wide Field Studies in the Southern Hemisphere: Resolved Stellar Populations of the Galactic Bulge and Magellanic Clouds. Astron. Soc. Pac., San Francisco, p. 366

Payne J. L., Filipović M. D., Reid W., Jones P. A., Staveley-Smith L., White G. L., 2004, MNRAS, 355, 44

Peck A. B., Goss W. M., Dickel H. R., Roelfsema P. R., Kesteven M. J., Dickel J. R., Milne D. K., Points S. D., 1997, ApJ, 486, 329

Pellegrini E. W., Oey M. S., Winkler P. F., Points S. D., Smith R. C., Jaskot A. E., Zastrow J., 2012, ApJ, 755, 40

Pennock C. M. et al., 2021, MNRAS, 506, 3540

Pietrzynski G. et al., 2019, Nature, 567, 200

Points S. D., Smith R. C., Chu Y. H., 2005, BAAS, 37, 1381

Schleicher D. R. G., Beck R., 2013, A&A, 556, A142

Shain C. A., 1959, in Bracewell R. N., ed., Proc. IAU Symp. 9 and Proc. URSI Symp. 1, Paris Symposium on Radio Astronomy. Stanford Univ. Press, Stanford, CA, p. 328

Siejkowski H., Soida M., Chyży K. T., 2018, A&A, 611, A7

Smith R. C., MCELS Team, 1999, in Chu Y.-H., Suntzeff N., Hesser J., Bohlender D., eds, Proc. IAU Symp. 190, New Views of the Magellanic Clouds. The Publications of the Astronomical Society of the Pacific, p. 28

Smith R. C., Points S. D., Chu Y. H., Winkler P. F., Aguilera C., Leiton R., MCELS Team, 2005, BAAS, 37, 1200

Stanimirovic S., Staveley-Smith L., Jones P. A., 2004, ApJ, 604, 176

Strong A. W., Mattox J. R., 1996, A&A, 308, L21

Subramanian S., Subramaniam A., 2015, A&A, 573, A135

Tabatabaei F. S., Beck R., Krügel E., Krause M., Berkhuijsen E. M., Gordon K. D., Menten K. M., 2007, A&A, 475, 133

Tabatabaei F. S., Krause M., Fletcher A., Beck R., 2008, A&A, 490, 1005

Tabatabaei F. S. et al., 2013a, A&A, 552, A19

Tabatabaei F. S., Berkhuijsen E. M., Frick P., Beck R., Schinnerer E., 2013b, A&A, 557, A129

Tabatabaei F. S. et al., 2017, ApJ, 836, 185

Tabatabaei F. S., Mínguez P., Prieto M. A. A., Fernández-Ontiveros J. A., 2018, Nat. Astron., 2, 83

Tingay S. J. et al., 2013, Publ. Astron. Soc. Australia, 30, e007

Valls-Gabaud D., 1998, Publ. Astron. Soc. Australia, 15, 111

van der Kruit P. C., 1971, A&A, 15, 110

van der Marel R. P., Kallivayalil N., 2014, ApJ, 781, 121

Vermeij R., van der Hulst J. M., 2002, A&A, 391, 1081

Vogt F. P. A., Seitenzahl I. R., Dopita M. A., Ghavamian P., 2017, A&A, 602, L4

Wayth R. B. et al., 2015, Publ. Astron. Soc. Australia, 32, e025

Weilbacher P. M., Streicher O., Palsa R., 2016, MUSE-DRP: MUSE Data Reduction Pipeline, Astrophysics Source Code Library, record ascl:1610.004

Weingartner J. C., Draine B. T., 2001, ApJ, 548, 296

Winkler P. F., Smith R. C., Points S. D., MCELS Team, 2015, in Points S., Kunder A., eds, ASP Conf. Ser. Vol. 491, Fifty Years of Wide Field Studies in the Southern Hemisphere: Resolved Stellar Populations of the Galactic Bulge and Magellanic Clouds. Astron. Soc. Pac., San Francisco, p. 343

Wong G. F., Filipovic M. D., Crawford E. J., de Horta A. Y., Galvin T., Draskovic D., Payne J. L., 2011a, Serbian Astron. J., 182, 43

Wong T. et al., 2011b, ApJS, 197, 16

Wong T. et al., 2017, ApJ, 850, 139

Yao J. M., Manchester R. N., Wang N., 2017, ApJ, 835, 29

This paper has been typeset from a TEX/LATEX file prepared by the author.